

CH-RUN: A ~~data-driven~~ deep-learning-based spatially contiguous runoff ~~monitoring product~~ reconstruction for Switzerland

Basil Kraft¹, Michael Schirmer², William H. Aeberhard³, Massimiliano Zappa², Sonia I. Seneviratne¹, and Lukas Gudmundsson¹

¹Institute for Atmospheric and Climate Science (IAC), ETH, Zurich, Switzerland

²Swiss Federal Research Institute (WSL), Birmensdorf, Switzerland

³Swiss Data Science Center, ETH, Zurich, Switzerland

Correspondence: Basil Kraft (basil.kraft@env.ethz.ch)

Abstract.

This study presents a data-driven reconstruction of daily runoff that covers the entirety of Switzerland over an extensive period from 1962 to 2023. To this end, we harness the capabilities of deep learning-based models to learn complex runoff-generating processes directly from observations, thereby facilitating efficient large-scale simulation of runoff rates at ungauged
5 locations. We test two sequential deep learning architectures, a long short-term memory (LSTM) model, a recurrent neural network able to learn complex temporal features from sequences, and a convolution-based model, which learns temporal dependencies via 1D convolutions in the time domain. The models receive temperature, precipitation, and static catchment properties as input. By driving the resulting model with gridded temperature and precipitation data available since the 1960s, we provide a spatiotemporally continuous reconstruction of runoff. The efficacy of the developed model is thoroughly assessed
10 through spatiotemporal cross-validation and compared against a distributed hydrological model ~~;-a model-~~ used operationally in Switzerland.

The developed data-driven model demonstrates not only competitive performance but also notable improvements over traditional hydrological modeling in replicating daily runoff patterns, capturing ~~annual-inter-annual~~ variability, and discerning long-term trends. The resulting long-term reconstruction of runoff is subsequently used to delineate ~~significant~~ substantial
15 shifts in Swiss water resources throughout the past decades. These are characterized by an increased occurrence of dry years, contributing to a negative decadal trend in runoff, particularly during the summer months. These insights are pivotal for the understanding and management of water resources, particularly in the context of climate change and environmental conservation. The reconstruction product is made available online.

Furthermore, the ~~reduced data dependency~~ low data requirements and computational efficiency of our model pave the way
20 for simulating diverse scenarios and conducting comprehensive climate attribution studies. This represents a substantial progression in the field, allowing for the analysis of thousands of scenarios in a time frame significantly shorter than traditional methods.

1 Introduction

Hydrological modeling and runoff prediction are critical for understanding and managing water resources, particularly in the face of climate change and increasing human impacts on the environment (Seneviratne et al., 2021; Arias et al., 2023). In Switzerland, a country characterized by diverse topography and climatic conditions, understanding and predicting runoff patterns is essential for effective water management, flood control, and environmental conservation (Brunner et al., 2019a).

~~While traditional~~ Traditional hydrological models offer pivotal insights into ~~land surface processes, they still exhibit uncertainties due to simplified process representations and~~ land surface processes. For Switzerland, a diverse array of hydrological models has been employed (Horton et al., 2022), ranging from complex ones, which are heavily founded on physical principles, to lightweight ones using conceptual process representations with calibrated parameters. While the former offer detailed insights and control, they rely on ~~parameters which are only marginally constrained by observations. Furthermore, they have a high demand of computational resources (Kraft et al., 2022).~~ a large number of inputs and are computationally expensive. The latter, in contrast, can be parsimonious in terms of data and computational resources, yet they need to be calibrated per catchment, which limits their applicability to prediction in ungauged catchments. The generalization to ungauged catchments via regionalization is possible, but introduces another layer of complexity (Beck et al., 2016). As a complementary approach, deep learning holds potential as a tool for hydrological modeling, both in terms of performance and efficiency (Nearing et al., 2021), and it comes with built-in regionalization when trained on multiple catchments jointly (Kratzert et al., 2024).

The ~~capability of data-driven modeling of~~ potential of machine learning to represent land surface processes ~~(Camps-Valls et al., 2021; Reichstein et al., 2018; Gauch et al., 2021a) via deep learning has been demonstrated before. For runoff modeling, its potential has mainly been explored for now- and forecasting, including runoff, has been widely demonstrated and discussed (Camps-Valls et al., 2021; Reichstein et al., 2018; Kraft et al., 2019; Gudmundsson and Seneviratne, 2015; Ghiggi et al., 2019, 2021; Muelchi et al., 2022). Deep learning, in particular, has shown promise for nowcasting and forecasting runoff at gauged catchments, for example, to enable warning systems of low or high flow aiding in warning systems for extreme flow events (Kratzert et al., 2018; Gauch et al., 2021a). It is, however, less common to employ data-driven models for large-scale reconstruction and monitoring (Nasreen et al., 2022). Reconstruction products are widely used for process understanding, investigation of long-term trends, and study of extreme events within a wider spatial and temporal context (Gudmundsson and Seneviratne, 2015; Ghiggi et al., 2019, 2021; Muelchi et al., 2022). In addition, machine learning-based models enable simulation of scenarios and real-time monitoring with significant speedup (Reichstein et al., 2019; Kraft et al., 2021).~~

This study introduces a data-driven approach to reconstructing daily runoff in Switzerland with contiguous spatial coverage, spanning an extensive period from 1962 to 2023 with the potential for continuous updates. ~~The extended coverage~~ We optimize a range of neural network-based models in different setups and evaluate their performance at the catchment-level in a comprehensive spatiotemporal cross-validation scheme. The results are benchmarked against simulations from the PREVAH hydrological model, which is used operationally in Switzerland. The extended coverage compared to PREVAH is enabled by reduced data requirements ~~;~~ by only using temperature and precipitation as meteorological drivers. In the Swiss context, these variables are available as regular grids since the 1960s, while additional variables, such as relative humidity and

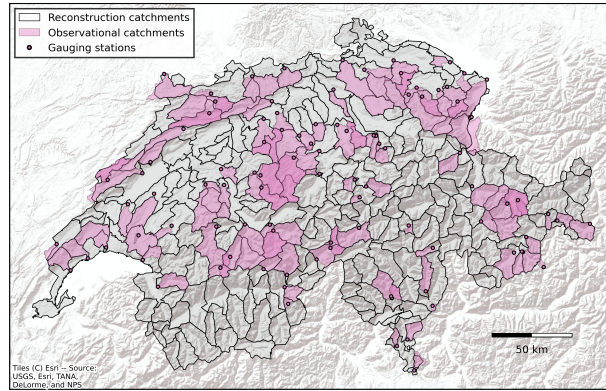


Figure 1. From sparse observations with low anthropogenic impact to contiguous spatial coverage. The 98 observational catchments highlighted in magenta were selected to only be marginally affected by anthropogenic factors and served as a base for training and evaluating the data-driven models. These catchments are of similar size as the target catchments for reconstruction (grey).

wind speed, are available starting in the 1980s. ~~We optimize a range of neural network-based models in different setups and evaluate their performance at the catchment level in a comprehensive spatiotemporal cross-validation scheme. The results are benchmarked against simulations from the PREVAH hydrological model, which is used operationally in Switzerland. The~~ The best-performing model is subsequently used to reconstruct daily runoff rates with complete spatial and temporal coverage since the 1960s. The paper closes with a discussion of the strengths and limitations of the approach and first insights from the extended reconstruction.

2 Data

2.1 Runoff observations

The observed discharges were taken from the CAMELS-CH dataset (Höge et al., 2023), which was updated with current data from the Swiss Federal Office for the Environment (FOEN, 2024) and supplemented by stations operated by the cantons Aargau, Baselland, Bern, St. Gallen and Zurich. In total, there were 267 stations available. A subset of 98 catchments was selected to minimize the anthropogenic impact (Fig. 1), i.e., no hydropower plant or reservoir was located upstream of the gauging station. This selection was based on the attributes of the CAMELS-CH dataset and insights from a previous study (Brunner et al., 2019c).

2.2 Meteorological drivers

We considered daily precipitation and air temperature as meteorological drivers, from interpolated observational data [with a spatial resolution of 1 km](#), namely the daily gridded datasets RhiresD (Schwarb, 2000; MeteoSwiss, 2021a) and TabsD (Frei, 2014; MeteoSwiss, 2021b). Gridded daily temperature and precipitation were spatially averaged for all considered catchments.

75 2.3 Catchment properties

For the across-catchment modeling of runoff, a set of static catchment properties was considered. These variables can improve generalization to catchments not seen during training. The static variables used are identical to those needed for forcing the spatially distributed PREVAH model (see next section) and include elevation, aspect, land use, soil depth, soil water holding capacity, hydraulic conductivity and two further indices describing soil and hydraulic properties. These gridded variables were aggregated to appropriate catchment values depending on the level of measurement, e.g., a circular mean for [slope-aspect](#) or a distribution of classes within each catchment for land use. As compared to previous applications of PREVAH (Viviroli et al., 2009b; Speich et al., 2015), the sources of the data providing the static properties has been updated and include:

- The swissALTI3D digital elevation model (swisstopo, 2018; Weidmann et al., 2018),
- the new habitat map of Switzerland (Price et al., 2023) aggregated to match the land use classes integrated in PREVAH,
- 85 – the Soilgrids products (Hengl et al., 2017; Poggio et al., 2021) enriched with high-resolution data for Swiss forests (Baltensweiler et al., 2022), merged and used to estimate soil properties, and
- the recent information on extent of glaciers in Switzerland (Linsbauer et al., 2021).

2.4 PREVAH runoff simulations as benchmark

The modelling of Swiss catchments has a long history in hydrology research (Horton et al., 2022; Addor and Melsen, 2019). Among a set of 21 models compared, Horton et al. (2022) found the PREVAH (PREecipitation-Runoff-EVApotranspiration Hydrological response unit model) model (Viviroli et al., 2009b) to be the most commonly used model with applications going from the plot scale process evaluation (Zappa and Gurtz, 2003), to the operational implementation for drought anticipation (Bogner et al., 2022), and to the Switzerland-wide assessment of climate impacts on hydrology (Brunner et al., 2019a). Furthermore, a PREVAH-based baseline is included in the Swiss version (~~Höge et al., 2023~~) of the CAMELS ([Höge et al., 2023](#)) data set (catchment attributes and meteorology for large-sample studies) as introduced by Addor et al. (2017).

For this study, we created a benchmark runoff simulation for the selected catchments on the basis of PREVAH. The simulations cover the period from 1981 until the end of 2022. The procedure adopted to obtain the PREVAH-benchmark closely follows the methodologies presented in previous studies (Speich et al., 2015; Brunner et al., 2019c; Höge et al., 2023). The gridded version of PREVAH (Viviroli et al., 2009b; Speich et al., 2015) has been applied at 500 m resolution. The time series of the investigated catchments were then obtained by spatially averaging daily gridded values. For further details on the setup

and application of PREVAH, we refer to the provided references above. For the present study it is nevertheless important to know that the gridded simulations at 500×500 m resolution have not been specifically re-calibrated for the catchments investigated. Instead, the spatially explicit version of PREVAH accesses a previously calibrated set of model parameters covering entire Switzerland which have been estimated using a regionalization approach (Viviroli et al., 2009c, a; Köplin et al., 2010).

105 We also note that runoff rates from PREVAH are to be considered as the natural response of the grids within the catchments investigated, without any considerations of water diversions for hydropower, flood damping by (regulated) lakes or any kind of water use (Brunner et al., 2019d).

3 Methods

3.1 Neural network architectures

110 We used two classes of temporal neural network models for runoff modeling, the long short-term memory model (LSTM, Hochreiter and Schmidhuber, 1997) and the temporal convolutional network (TCN, Bai et al., 2018). While the LSTM maintains an internal state that is updated dynamically, the TCN is based on a sparse and efficient 1D-convolution in the time domain. The latter is parallelizable in time and therefore computationally more efficient. We employ three approaches, described hereafter, to fuse the dynamic meteorological variables $\mathbf{x}_{t,c}$ at time t and catchment c , with the static variables \mathbf{s}_c , independent of the temporal model used. The selection of the best fusion approach was part of the hyperparameter tuning (Sect. 3.3) and was performed independently of the model setup described in [See Sect. 3.5](#). Note that the following description of the model architectures is simplified and that the actual setup uses vectorized and efficient computation.

115

3.1.1 Prefusion with encoding

In the first approach, which we called ~~prefusion with encoding~~[prefusion with encoding](#), $\mathbf{x}_{t,c} \in \mathbb{R}^M$ (a vector of M meteorological features) and $\mathbf{s}_c \in \mathbb{R}^S$ (a vector of S static features) are, as part of the model training, encoded into $\mathbf{e}_{t,c} \in \mathbb{R}^D$, i.e., into a vector of length D (the model dimensionality). The encoding is done using stacked feed-forward neural network layers f_{NN_1} and f_{NN_2} , respectively. The two encodings are combined by element-wise addition, i.e., static encoding is added to each meteorological encoding equally, as shown in Eq. (1). The resulting combined encoding $\mathbf{e}_{t,c}$ is then fed into one or multiple temporal layers f_{TNN} (Eq. (2)), yielding the temporal encoding $\mathbf{h}_{t,c} \in \mathbb{R}^D$, which is then decoded into a single value $q_{t,c}^* \in \mathbb{R}$ (Eq. (3)) by another stack of feed-forward neural networks f_{NN_3} .

120

125

$$\text{feature encode} \quad \mathbf{e}_{t,c} = f_{\text{NN}_1}(\mathbf{x}_{t,c}) + f_{\text{NN}_2}(\mathbf{s}_c) \quad (1)$$

$$\text{temporal encode} \quad \mathbf{h}_{t,c} = f_{\text{TNN}}(\mathbf{e}_{t,c}, \mathbf{e}_{t-1,c}, \dots, \mathbf{e}_{t-k,c}) \quad (2)$$

$$\text{output decode} \quad q_{t,c}^* = f_{\text{NN}_3}(\mathbf{h}_{t,c}) \quad (3)$$

$$\text{output transform} \quad q_{t,c} = \log(1 + \exp(q_{t,c}^*)) \quad (4)$$

130 While the LSTM uses all input time-steps, the TCN uses limited context k , depending on its hyperparameters. The decoded output is then transformed to the positive domain, $q_{t,c} \in \mathbb{R}_+$, using the Softplus activation, as shown in Eq. (4). This output mapping is consistent across the fusion methods.

In this fusion approach, the potentially complex interactions of the dynamic and static input variables are injected prior to the temporal layer, presumably unloading some of the non-temporal interaction complexity from it. Note that the selection of
135 model characteristics, such as number of hidden nodes and layers, was based on hyperparameter tuning (see next section).

3.1.2 Prefusion with repetition

In the second approach, ~~prefusion with repetition~~prefusion with repetition, the static vector s_c is simply repeated in time and concatenated to the temporal input $x_{t,c}$ (Eq. (5)). This combined encoding, based on a feed-forward neural network f_{NN_4} , is then fed into the temporal module Eq. (6) and mapped to the output with another neural network f_{NN_5} as previously described
140 and as shown in Eq. (7) and Eq. (8). This approach is conceptually similar to prefusion with encoding, but it leaves the learning of the non-linear interactions within the static inputs to the temporal layer.

$$\text{feature encode } e_{t,c} = f_{\text{NN}_4}([x_{t,c}, s_c]) \quad (5)$$

$$\text{temporal encode } h_{t,c} = f_{\text{TNN}}(e_{t,c}, e_{t-1,c}, \dots, e_{t-k,c}) \quad (6)$$

$$\text{output decode } q_{t,c}^* = f_{\text{NN}_5}(h_{t,c}) \quad (7)$$

$$145 \text{ output transform } q_{t,c} = \log(1 + \exp(q_{t,c}^*)) \quad (8)$$

3.1.3 Postfusion with repetition

~~Postfusion with repetition~~Postfusion with repetition, finally, first encodes the meteorological input $x_{t,c}$ (Eq. (9)) with a feed-forward neural network f_{NN_6} , runs the encoding through the temporal module (Eq. (10)), and then decodes the combined temporal encoding and static inputs s_c via repetition in time (Eq. (11)) by f_{NN_7} , followed by the mapping to the positive
150 domain (Eq. (12)). In this approach, the dynamics learned by the temporal layers cannot be modulated by the static variables.

$$\text{feature encode } e_{t,c} = f_{\text{NN}_6}(x_{t,c}) \quad (9)$$

$$\text{temporal encode } h_{t,s} = f_{\text{TNN}}(e_{t,c}, e_{t-1,c}, \dots, e_{t-k,c}) \quad (10)$$

$$\text{output decode } q_{t,c}^* = f_{\text{NN}_7}([h_{t,c}, s_c]) \quad (11)$$

$$\text{output transform } q_{t,c} = \log(1 + \exp(q_{t,c}^*)) \quad (12)$$

155 3.2 Model training and hyperparameter tuning

3.2.1 Data transformation

We transformed both the dynamic and static input features using z -transformation to have zero mean and unit variance. This process was executed individually for each cycle of cross-validation (see Sect. 3.4) and based on the specific training set

assigned to that cycle. To maintain the target variable, i.e., runoff, within a positive range, its values were adjusted through
160 normalization by dividing the values by the global 95th percentile value derived from the training set.

3.2.2 Model optimization

The model parameters were updated using standard backpropagation (Amari, 1993) with the AdamW optimizer (Loshchilov
and Hutter, 2019), a stochastic gradient descent method with adaptive first-order and second-order moments. As objective
function, we used the mean squared error (MSE), defined as $\mathcal{L}_{\text{MSE}} = \frac{1}{TC} \sum_{c=1}^C \sum_{t=1}^T (y_{t,c} - \hat{y}_{t,c})^2$, where $y_{t,c}$ is the normalized
165 observation and $\hat{y}_{t,c}$ the respective predicted runoff at time t of T number of time steps and catchment c among C catchments.
Optionally, we considered square root-transformed prediction and target to reduce the right-skewness of the distribution and
therefore to facilitate the training.

The training sets were constructed with the goal to ensure equal representation of each catchment, regardless of the number
of observations available from each. To do this, we iteratively selected samples from each catchment in a randomized order.
170 We refer to one complete iteration through all catchments as an “epoch”. For each catchment, a two year period was randomly
selected, ensuring at least 30 days of runoff data were present. Additionally, a one-year lead-in period was introduced for model
spin-up, which was not factored into the optimization calculations.

Throughout the model training phase, we used mini-batches of 32 samples. A mini-batch is a subset of the training data
used in each step of the gradient descent process to update the model’s parameters. This approach strikes a balance between
175 computational efficiency and the stochastic nature of the training, allowing more frequent updates and efficient use of par-
allel processing. For validation and testing, the complete time series was processed in each evaluation epoch, optimizing for
efficiency since no parameter updates were needed in these phases.

3.3 Hyperparameter tuning

Hyperparameter tuning, an essential step in enhancing a deep learning model’s performance, was systematically conducted.
180 This involves identifying the best combination of pre-set parameters, like the learning rate or the number of neurons per layer,
to optimize model performance. We ~~used~~ [referred to Appendix A1 for a comprehensive list of hyperparameters used. We used](#) the
initial cycle of our cross-validation (see Sect. 3.4) process for this tuning. The hyperparameters were tuned using the Optuna
framework (Akiba et al., 2019). After the evaluation of 15 random hyperparameter combinations, 45 further configurations
were suggested iteratively using a Bayesian surrogate model based on the Tree-structured Parzen Estimator (TPE) algorithm
185 (Bergstra et al., 2011). As some configurations may perform badly in the early training phase, we used hyperband pruning to
stop such unpromising runs early on without wasting resources (Li et al., 2018). With the optimal hyperparameters determined,
we completed the full cross-validation process, described in the next section.

3.4 Cross-validation

We carefully designed a k -fold cross-validation setup for a fair model evaluation and to assert the high quality of the final reconstruction product. The 98 training catchments were randomly divided into $k = 8$ sets and iterated over such that each set was used as validation and testing once, respectively (Fig. 2a). While the training data is used for optimizing the model and validation data is used to monitor model generalization during training, the test data serves for the final model evaluation. The remaining 169 catchments, which are more impacted by anthropogenic factors, were optionally used as additional training catchments – but never to evaluate the model. In addition, the time domain was split into training, validation, and test periods (Fig. 2b). These periods were kept fixed during cross-validation. The temporal splitting was chosen to be representative of the model’s temporal interpolation and extrapolation skills. At the same time, the validation and test periods should contain minimal missing data, to not give more emphasis to catchments with more observations. Therefore, we selected two five-year blocks of test data, one from (the beginning of) 1995 to (the end of) 1999, and one from 2016 to 2020. The test ranges were separated from the training set to ensure minimal data leakage. This relates to the fact that autocorrelation in time series data can lead to overfitting because it causes models to mistake random patterns in the data as significant. In addition, the buffer added after every temporal block avoids overlapping of the test set spin-up period of one year with the training set, which would again encourage overfitting. Note that the validation set was not separated by a buffer from the training set in order to not discard any observations and because the final evaluation was done on the test set. Overall, the spatial and temporal data splitting was a trade-off between computational and autocorrelation requirements, and data limitations.

In each of the k iterations, six catchment sets were used for training, i.e., for optimizing the neural network parameters, while one set was used for validation and one was held out for testing. After an epoch, i.e., one full iteration through the training data, the loss was computed on the validation set. The loss was monitored and training was interrupted if the loss on the validation set was getting worse over a given number of epochs (the “patience”). The best model in terms of the validation loss was then restored and used for prediction on the test set. This routine is called “early stopping” and reduces overfitting (Yao et al., 2007). The final predictions on the test set were then used for model evaluation. As each catchment set was the test set once, we obtained independent test predictions for each of the 98 catchments.

3.5 Factorial ~~experiments on experiment and model architecture evaluation~~

In this section, we describe the model setups tested in a factorial experiment and the model evaluation. We selected the best-performing model based on the median Nash-Sutcliffe modeling efficiency (NSE, Nash and Sutcliffe, 1970) across catchments, evaluated on the test set. The NSE as defined in Eq. (13), is calculated on catchment level:

$$\text{NSE} = 1 - \frac{\sum_{t=1}^T (y_t - \hat{y}_t)^2}{\sum_{t=1}^T (y_t - \bar{y})^2}, \quad (13)$$

where y_t is the observed and \hat{y}_t the ~~predicted-simulated~~ runoff at time t of T total time steps, and \bar{y} is the mean of the observed time-series. The NSE can take values from $-\infty$ to 1, where values above 0 mean that the predictions are better than taking the mean of the observations, and 1 means perfect prediction. Note that the NSE is closely related to the R-squared, but the NSE

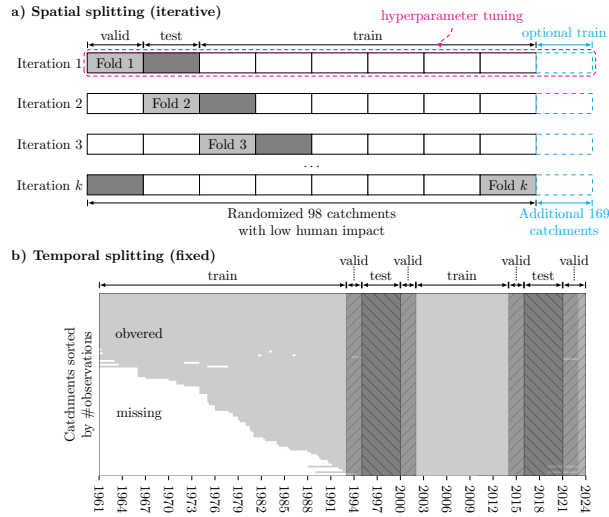


Figure 2. Cross-validation scheme: Panel a) shows the spatial domain, consisting of 98 catchments in Switzerland, which we randomly divided into $k = 8$ sets. These sets were used iteratively, allowing each to serve as a validation and test set once. Catchments significantly affected by human actions were included in the training phase optionally to enrich model learning, but they were consistently excluded from the validation and test phases to maintain the focus on natural runoff patterns. In Panel b), the time domain is delineated into fixed training, validation, and test periods. The used sets are the intersections of these spatial and temporal splits. With the initial iteration, hyperparameter (HP) tuning was performed, and the best HPs identified were then applied in subsequent cross-validation steps. By evaluating the model on the test sets, we comprehensively assessed the model’s skill in generalizing across both spatial and temporal dimensions.

220 normalizes the sum of the squared residuals by the catchment variance instead of the global variance. Hence, the NSE does not give more emphasis to catchments with larger variance and is, therefore, also sensitive to catchments with low dynamic range.

3.6 Model evaluation

225 To better understand the error structure, we also evaluate the MSE decomposition into bias, variance, and phase error (Kobayashi and Salam, 2012) where μ is the mean and σ is the standard deviation of the simulations s and the observations o , and r is the linear correlation coefficient between them. The squared bias reflects the model fit in terms of average and the variance error in terms of the scale. The phase error can be interpreted as a measure of reproducing the timing, i.e., how well the dynamics are matched regardless of bias and scale.

Different model setups were tested in ~~factorial experiments~~ a factorial experiment, and each combination of the factors was evaluated. A first factor determines the temporal component of the overarching model architecture: {LSTM, TCN}. ~~We also tested whether transforming~~ A next factor determines whether the target variable and predictions are transformed using the square root, in order to reduce the skewness of the ~~runoff distribution, or no transformation~~ distribution: { T_{none} , T_{sqrt} }. We tested the usage of the 169 optional catchments (267 in total) in the training set, compared to the 98 only (Fig. 2a): { C_{98} , C_{267} }. The

last factor concerns the usage of static input variables. Due to the relatively large number of catchment properties (28), we alternatively used dimensionality-reduced static features. Using principle component analysis (PCA, Wold et al., 1987), all static features except catchment area were compressed into 5 components, which represent 66%-% of the variance. Catchment area was always used as a separate static input, as we consider it to be a key input feature. Hence, we either use catchment area only, a dimensionality-reduced version off the static variables using PCA, or all static variables described in the data section: $\{S_{\text{area}}, S_{\text{PCA}}, S_{\text{all}}\}$.

This yields a total of 24 models, and for each of them, independent hyperparameter tuning and cross-validation was performed. Note that the fusion strategy for static and dynamic features introduced in Sect. 3.1 was part of the hyperparameter tuning, and not considered as a factor here.

To better understand the error structure, we also evaluate the MSE decomposition into bias, variance, and phase error (Kobayashi and Salam, 2000; Gupta et al., 2009):

$$e_{\text{MSE}} = \overbrace{(\mu_{\hat{y}} - \mu_y)^2}^{e_{\text{bias}}} + \overbrace{(\sigma_{\hat{y}} - \sigma_y)^2}^{e_{\text{variance}}} + \overbrace{2\sigma_{\hat{y}}\sigma_y(1-r)}^{e_{\text{phase}}} \quad , \quad (14)$$

where μ is the mean and σ is the standard deviation of the simulations \hat{y} and the observations y , and r is the linear correlation coefficient between them. The squared bias e_{bias} reflects the model fit in terms of average and the variance error e_{variance} in terms of the scale. The phase error e_{phase} can be interpreted as a measure of reproducing the timing, i.e., how well the dynamics are matched regardless of bias and scale.

3.6 Runoff reconstruction

To achieve a complete contiguous reconstruction from 1962 to 2023 for the small to medium-sized catchments with national coverage (Fig. 1), we used the best-performing model from the cross-validation. The best model was selected based on median test set NSE across catchments. From the ensemble members from the eight-fold cross-validation, we obtained eight reconstructions with full coverage, of which we use the median (average of the two middle values) as the final data product. The year 1961 was removed from the reconstruction as it ~~serves~~ served as spin-up.

4 Results

4.1 Catchment level performance and benchmarking

In this section, we evaluate the model performance at catchment level and compare the data-driven models. All analysis is, unless stated otherwise, based on the test set (Fig. 2), i.e., spatially and temporally distinct data. Due to the iteration over the catchment groups in the cross-validation, each catchment was in the test set one time. The fixed splitting of the time domain, however, restricts our evaluation to the test periods, i.e., January 1995 to December 1999, and January 2016 to December 2020. Throughout the evaluation, we use the hydrological model PREVAH as a benchmark.

4.1.1 Comparison of model setups Model performance

We first evaluate how the different model architectures (LSTM and TCN), setups, and hyperparameters affected model performance. In Fig. A1, the diagonal shows how the model setups impacts the median NSE across catchments, and the offset triangular shows the interactions of the factors.

Understanding To understand the capabilities of our model ~~necessitates a thorough evaluation of daily runoff simulations to represent daily runoff at catchment level, we evaluate the model performance first~~. Figure 4.1.2 presents the empirical cumulative density functions for different metrics across the 98 ~~training~~ catchments. Models based on the TCN architecture are depicted in blue, those using LSTM networks in red, and the PREVAH model is represented in black. The model with the best performance is emphasized using a thicker line. Panel a focuses on the Nash-Sutcliffe Efficiency (NSE), while panels b–d provide a detailed breakdown of the Mean Squared Error (MSE) into its components – squared bias, variance error, and phase error – as previously introduced.

Overall, we observed a large variance in performance across model setups in terms of catchment-level NSE, and the TCN-based models performed worse than the LSTM in general. This is mainly due to the two best-performing LSTM models (also see model-wise NSE in Appendix A, Tab. A2 & A3). The best-performing LSTM (LSTM_{best}) achieved a median NSE of 0.76. The MSE decomposition shown in Fig. 4.1.2b–d indicates that the LSTM_{best} (thick red line) is among the best models in terms of all error components. The phase error ~~contributes contributed~~ most to the overall error by a wide margin, signifying that representing the timing of the runoff is more challenging than representing the average and the scale.

The best-performing ~~model was the LSTM (“LSTM_{best}”) with the setup {S_{all}, C₂₆₇, T_{sqrt}}~~ setup was {LSTM, S_{all}, C₂₆₇, T_{sqrt}}, i.e., ~~the setup~~ with all static features, additional training catchments, and with square root transform of the target, paired with the LSTM architecture. This model performed only marginally better than ~~the LSTM model setup {S_{area}, C₂₆₇, T_{sqrt}}~~ {LSTM, S_{all}, C₉₈, T_{sqrt}} i.e., the one ~~with only area as static variable, not using the additional catchments for training. These models both worked best with the prefusion with encoding approach (see Sect. 3.1).~~ An overview of all model setups and their performance is provided in Appendix A, ~~Tab. A2 & A3~~ A1, and a short discussion of the factorial experiment can be found in Appendix A2.

The PREVAH model achieved ~~an a median~~ NSE of 0.72 (Fig. 4.1.2a), which is marginally lower than LSTM_{best} (NSE of 0.76), yet better than some of the other data-driven models. The PREVAH model ~~shows showed~~ similar bias and variance error (Fig. 4.1.2b–d) to those of LSTM_{best} in terms of the median, yet it seems to be more robust in representing these aspects, as the LSTM_{best} lags behind in the larger errors. Regarding the phase error, in contrast, the data-driven models in general and the LSTM_{best} in particular clearly ~~outperform outperformed~~ PREVAH across catchments.

Next, we investigate the spatial distribution of the errors. First, we notice that the performance of LSTM_{best} in terms of NSE, shown in the top-left panel Fig. 4, does not exhibit a clear spatial pattern. Yet, the model seems to struggle with some particular catchments. Interestingly, these are the very catchments where PREVAH outperformed LSTM_{best} clearly (compare Fig. 4 top-left panel dark blue values to lower-left panel dark red values).

To understand how this spatial patterns are linked to catchment properties, we performed an exploratory analysis. First, we identified the tails of the distributions (inset histograms in Fig. 4, and PREVAH performance, not shown) using the 10th and

90th percentiles. We then compared properties of catchments in the tails to the “normal” group (between the 10th and 90th percentiles) using the two-sided, non-parametric Mann-Whitney U test with a significance level of $\alpha = 0.1$ (?). The analysis was restricted to a subset of catchment properties: mean and variance of runoff, elevation, catchment area, and water body fraction. Here, we report the most notable findings from this ad-hoc analysis.

300 For LSTM_{best}, poor performance (NSE below 0.14) was observed in catchments with low runoff mean and variance, whereas good performance (NSE above 0.86) was achieved in catchments with high runoff variance. Similarly, PREVAH struggled (NSE below 0.08) in catchments with low runoff mean and variance, as well as in low-elevation and lake-dominated conditions, but performed well (NSE above 0.84) in catchments with high runoff mean, large catchment areas, and minimal lake presence. As expected, the bias of LSTM_{best} was low in catchments with low runoff mean and variance, with variance error increasing
305 in high runoff variance conditions. Phase error for LSTM_{best} was lowest in catchments with low runoff mean and variance and large catchment area.

Significant differences in NSE performance between the two models were observed in catchments with low runoff variance. PREVAH outperformed LSTM_{best} (NSE improvement above 0.28) in catchments with both low runoff mean and variance. Conversely, LSTM_{best} clearly outperformed PREVAH (NSE improvement above 0.28) in low-elevation, lake-dominated catchments
310 that also had low runoff variance.

4.1.2 Annual variability and trends

For a reconstruction product, it is crucial to adequately represent yearly variability and long-term trends. We, therefore, evaluate this aspect on annual runoff aggregates (Fig. 5). The best-performing model, LSTM_{best}, ~~represents~~ represented the interannual variability (Fig. 5a), quantified as the Pearson correlation coefficient between the annual values for each catchment, well with
315 a median of $r = 0.93$, and with 75% ~~%~~ of catchments above $r = 0.85$. The ~~global bias is~~ bias averages close to zero and for 50% ~~%~~ of the catchments, it ~~is~~ was in the range of ~~-0.5 to 0.5~~ -250 to 250 mm y⁻¹ (Fig. 5b). On the interannual variability, PREVAH ~~shows~~ showed a slightly lower correlation (Fig. 5a) across catchments with a median of ~~$r = 0.92$~~ $r = 0.91$. In terms of bias, PREVAH ~~seems to do marginally worse in terms of median bias, but overall the biases have a smaller~~ performed marginally better with a median closer to zero and a lower spread (Fig. 5b).

320 Figure 5c illustrates how the models ~~capture~~ captured spatial patterns of annual trends between January 1995 and December 2020 (Fig. 5c). The agreement was calculated by first computing the catchment-level linear trends for the observations and the simulations ~~independently by~~ PREVAH and LSTM_{best} independently using the robust Theil-Sen estimator (Sen, 1968). Then, ~~a linear regression was fit between observed and simulated trends. A large correlation indicates a good fit of the spatial patterns. The~~ we fit a regression between the observed and estimated trend slopes by the two models using robust regression
325 with Huber weighting and the default tuning constant of $c = 1.345$ (Huber and Ronchetti, 2009). This approach reduces the impact of outliers by giving lower weight to large residuals. For quantifying the alignment of the simulated trends, we use Spearman correlation (ρ), which is relatively robust against outliers. While the LSTM_{best} ~~represents~~ represented the spatial patterns of the linear trend relatively well with a ~~Pearson correlation of $r = 0.77$. The model does, however, underestimate the negative trends with a slope of 0.84 and a bias of -0.01.~~ The PREVAH model represents the spatial pattern worse with an

330 $r = 0.60$, and it overestimates the trends slightly (slope of 1.07), while the bias is again -0.01 . The representation of the trends
across catchments are, however, not significantly different between correlation of $\rho = 0.60$, PREVAH achieved a correlation
of $\rho = 0.42$. Both models underestimated the strength of negative and positive trends with slopes of 0.52 (LSTM_{best}) and 0.64
(PREVAH), and they exhibited small negative biases of -3.73 (LSTM_{best} and PREVAH on the basis of a significance level of
 $\alpha = 0.05$ ($p_{\text{bias}} = 0.281$, $p_{\text{slope}} = 0.056$)) and -6.44 (PREVAH) mm y^{-1} .

335 4.2 Qualitative evaluation of selected catchments

To understand how the models represent different hydrological regimes, we perform a qualitative comparison for a selection
of catchments. We selected single catchments that are either dominated by a) rainfall, b) lakes, c) snow, or d) glaciers for this
purpose (Fig. 6). These example catchments serve as means for qualitative model comparison, and we do not expect these
insights to directly generalize across catchments.

340 The rainfall-dominated catchment, the Murg at Frauenfeld (ID: 2386), is located in the Northwest of Switzerland on the
Swiss Plateau, with an area of $\sim 200 \text{ km}^2$ and an average elevation of $\sim 600 \text{ m}$. Maximum snow water equivalent (SWE) has
been below 80 mm in the past years (Höge et al., 2023) and was not considered to affect runoff for most days of the year. The
lake-dominated catchment, the Aabach at Hitzkirch (ID: 2416), is located in the central Pre-Alps, with an area of $\sim 70 \text{ km}^2$
and an average elevation of $\sim 600 \text{ m}$. The gauging station is located just a few hundred meters after the outflow of the $\sim 5 \text{ km}^2$
345 Lake Baldegg, which damps runoff peaks and also affects the low flow regime. The snow-dominated catchment, the Plessur at
Chur (ID: 2185), is located in the Eastern Swiss Alps, with an area of $\sim 250 \text{ km}^2$ and an average elevation of $\sim 1900 \text{ m}$ (from
 $\sim 500 \text{ m}$ to $\sim 3000 \text{ m}$). Maximum SWE varied in the past 25 years between 200 and 500 mm. There are no large glaciers in
this area which could influence runoff. The glacier-dominated catchment, the Simme at Oberried/Lenk (ID: 2219), is located
in the Western Swiss Alps, with an area of 35 km^2 and an average elevation of $\sim 2300 \text{ m}$ (from $\sim 1000 \text{ m}$ to $\sim 3200 \text{ m}$). About
350 ~~25%~~ % of the area is covered by glaciers. Maximum SWE varied in the past 25 years between 400 and 1100 mm.

For the rainfall-dominated catchment, PREVAH and LSTM_{best} ~~show~~ showed similar behavior (Fig. 6a) and both models
~~can~~ could reproduce the runoff peaks and overall patterns. For the lake-dominated catchment, the LSTM_{best} outperformed
the PREVAH model in terms of NSE (Fig. 6b). Visual inspection shows high peaks in PREVAH simulations, which indicate
missing buffering dynamics in lakes. This is not surprising, as PREVAH does not represent lakes explicitly, while the LSTM
355 can learn the buffering implicitly via the catchment properties, among which the fraction of water bodies may be the most
relevant one. For the snow-dominated catchment shown in (Fig. 6c), the PREVAH model ~~manages~~ managed to represent the
runoff processes better in 1998, and similar in the year of 2018. Here the LSTM_{best} overestimates runoff in general, and
particularly peaks in the summer. Snow melt responds strongly to radiation, which was not included as a driver of the LSTM.
Further, snow-related processes are spatially heterogeneous, depending on elevation and exposition. The lumped LSTM model
360 cannot resolve these processes at sub-catchment level, while the PREVAH model operates on a high-resolution grid. Although
worse in terms of NSE, the LSTM ~~manages~~ managed to better represent the snow melt in 2018, possibly because snow was
already melted away in the PREVAH simulation. In a glacier-dominated catchment, finally, LSTM_{best} ~~represents~~ represented
the runoff patterns slightly better than PREVAH.

4.3 Runoff reconstruction

365 The reconstruction of daily runoff from 1962 to 2023, referred to as CH-RUN, was conducted with the best-performing model based on prior analysis. The final estimate was calculated as the median across the eight ensemble members from the cross-validation. Figure 7 shows the annual runoff as quantiles relative to the reference period from 1971 to 2000. The quantiles were calculated per catchment comparing the annual values to the empirical distribution of the reference period. Turquoise colors indicate that, for a given catchment, the yearly average runoff is rather large compared to the reference, and brown colors
370 signify dry years.

The reconstruction suggests that dry years with similar amplitude compared to the conditions of the 21st century were already present in the 1960s and 70s (e.g., in 1964 and 1976). However, the frequency of dry years increased significantly – and that of wet years substantially decreased – according to the model estimates.

Figure 8 shows the annual national runoff anomalies and corresponding trends for CH-RUN. According to the CH-RUN
375 reconstruction, the recent dry conditions are matched by values in the 1960s and 70s in terms of amplitude, while the frequency of dry years increased, and that of wet years decreased. Extremely dry years (exceeding the 0.1 quantile of the reference period) were absent in the 1980s and 90s, while wet years (exceeding the 0.9 quantile of the reference period) were more frequent during this period. The last extremely wet year occurred 1999, and the driest year was 2022.

In Fig. 9, the decadal mean values are disaggregated into seasonal patterns. Here, average annual sums across decades are
380 shown, again relative to the reference period from 1971 to 2000. The decadal means again point at strong trends towards less runoff at yearly scale. In the winter months December to February (DJF), we see a slight tendency towards less runoff north of the Alps, while the 2020s exhibit more runoff in the Pre-Alps. From March to May (MAM), northern Switzerland, the Pre-Alps, and the canton of Ticino, show a clear trend towards drier conditions. Even more pronounced, June to August (JJA) reveal a tendency towards less runoff in the central Alps with higher altitudes and the canton of Ticino. From September to
385 November (SON), the patterns are again less distinct, yet there is a general trend towards drier conditions in most catchments.

5 Discussion

5.1 Neural network architectures and the role of data

The better performance of the LSTM compared to the TCN (Fig. 4.1.2) is somewhat surprising, as the latter has been reported to perform well in time series prediction settings (e.g., Zhao et al., 2019; Catling and Wolff, 2020; Yan et al., 2020). The difference
390 in performance can be traced back to the two best-performing LSTMs (Fig. 4.1.2, Tab. A2 & A3) and hint at better capabilities of the LSTM to represent interactions between meteorological and static features, under these data-limited conditions. It seems that the LSTM is more data-efficient than the TCN, which is also supported by the lower number of tunable parameters used by the former. ~~It might be therefore~~ (see Tab. A2 & A3). It might therefore be possible that the TCN can compete with the LSTM architecture if more training data is available. Other deep learning approaches for modeling time series exist, among
395 which transformer-based architectures (Vaswani et al., 2017) became popular recently (Lim et al., 2021; Zhou et al., 2021;

Xu et al., 2023). Due to the powerful and complex encoder-decoder structure, these models unfold their potential especially in forecasting settings and with large amounts of training data. Given the relatively low amounts of training data available for the study domain, we do not expect significant improvement by using such architectures. Nevertheless, exploration of this architecture may hold potential for improved reconstruction in the future.

400 In runoff modeling, integrating catchment properties with meteorological features is a prevalent approach (e.g., Kratzert et al., 2019). We found that the most effective data fusion method involved channeling static variables through the LSTM's temporal layers while handling some non-temporal interactions in an upstream encoding layer. Our LSTM successfully learned the complex interactions between static and meteorological features, extending its applicability to untrained catchments and time ranges. Enhancing the model's predictions was achieved by incorporating a broader range of catchments and fully utilizing
405 catchment properties (Fig. A1), acknowledging that a wider input feature space necessitates more data. This finding aligns with our previous diagnosis of spatial information limitations due to the relatively small number of training catchments. Although the importance of data has been well reported (Kratzert et al., 2018; Gauch et al., 2021b), these results reaffirm the value of additional data in enhancing model performance. Consequently, we recommend exploring methods to incorporate more training data, such as transfer learning from other tasks (Sadler et al., 2022) or other regions (Pan and Yang, 2010; Yao et al., 2023; Xu et al., 2023), for example from large-scale datasets (Kratzert et al., 2023; Do Nascimento et al., 2024), and considering
410 alternative data sources like [citizen-science-projects-bottom-up data mobilization efforts](#) (Do et al., 2018; Gudmundsson et al., 2018; Nardi et al., 2022; Kebede Mengistie et al., 2024) as promising avenues for future research.

It is encouraging to see that the LSTM did manage to implicitly learn complex runoff dynamics across hydrological regimes (Fig. 6). The data-driven model has learned buffering effects by lakes and, to a certain extent, runoff-generating processes
415 related to snow and, possibly, also glaciers. Similar behavior has been reported before. Kratzert et al. (2019) and Lees et al. (2022), for example, reported that an LSTM was able to represent long-term snow dynamics. We expect potential for improvement by better representing buffering processes via routing of the runoff (Bindas et al., 2024) and by an improved representation of snow and glacier processes. This can be achieved via the combination of physically-based and data-driven modeling (Reichstein et al., 2019), e.g., by directly employing physical constraints in an end-to-end hybrid physics-machine learning setup
420 (Kraft et al., 2022, 2020; Höge et al., 2022), by penalizing physically implausible simulations during training (Daw et al., 2021), or by regularizing the model with auxiliary tasks (Sadler et al., 2022), to only name a few.

5.2 Comparison with the PREVAH model

Although some neural networks outperform the PREVAH model (Fig. 4.1.2), the differences in terms of NSE were small. The marginally better representation of runoff mean and amplitude by PREVAH make sense intuitively, as the data-driven
425 model has a very limited number of training catchments to learn spatial features from. Equivalently, the better representation of temporal patterns by the LSTM could be explained by the fact that [the LSTM-it has access to long time-series to learn the dynamics from. The sole fact that deep-It is not surprising that machine learning can outperform physically-based models is not surprising in runoff prediction.](#) as this has been demonstrated [before \(e.g., Kratzert et al., 2018; Lees et al., 2021\) in previous studies \(e.g., Kratzert et al., 2018; Lees et al., 2021; Gudmundsson and Seneviratne, 2015; Ghiggi et al., 2021\)](#). However, in this

430 study, we used a limited amount of meteorological drivers compared to the needs of the PREVAH model. Furthermore, the PREVAH model is an expert model that is using carefully regionalized parameters for the study domain (Viviroli et al., 2009c). As PREVAH is providing the natural discharge within the catchments domain, it is not able to capture the dampening effect provided by lakes (~~ID-2416 in~~ Fig. 6b). The LSTM is able to cope with such effects as part of its global calibration result.

435 From the analysis of the spatial patterns of the model performance (Fig. 4), we learned that the LSTM_{best} encountered challenges with dry catchments that have both low runoff mean and variance. This was not surprising due to the high signal-to-noise ratio in runoff observations and the sensitivity to minor variability in the meteorological variables and catchment properties in dry catchments. Similarly, PREVAH struggled with dry conditions, but still it performed clearly better under such conditions. In contrast, LSTM_{best} represents lake-dominated catchments with low elevation significantly better. This was expected, as PREVAH does not represent lake processes, and therefore, it cannot properly represent their dampening effect. The interaction
440 with elevation could be explained by the fact that the largest lakes in Switzerland are at medium-to-low elevation.

The PREVAH model is already used successfully for reconstruction (Otero et al., 2023) and future climate scenarios (Laghari et al., 2018; Brunner et al., 2019b). With the objective of real-time monitoring, long-term reconstruction, and potentially an efficient simulation of climate scenarios in mind, we consider the similar performance compared to the benchmark sufficient. The similar capability to representing interannual patterns by the LSTM_{best} and the slightly better fidelity of trends (Fig. 5)
445 is, especially given the lowered data requirements, encouraging. We want, however, to state here upfront that a process-based hydrological model has advantages over a data-driven model, such as interpretability and physical consistency.

5.3 Plausibility of the runoff reconstruction product

The reconstruction of runoff back to the early 1960s for Switzerland is a novelty enabled by the reduced data needs of our deep learning-based approach compared to the PREVAH model. Here, we evaluate the plausibility of the ~~observed-simulated~~
450 patterns based on Fig. 7-9 by contrasting them to prior knowledge.

The overall trend towards drier conditions simulated by our data-driven model aligns with independent studies. This has been reported widely for Europe (Orth and Destouni, 2018; Hanel et al., 2018) and Switzerland specifically (Hohmann et al., 2018; Brunner et al., 2019b; Henne et al., 2018). Interestingly, the results reveal that the runoff anomalies of the 2022 drought (e.g., Toreti et al., 2022; Schumacher et al., 2024) were larger than that of the well-documented 2003 drought (e.g., Ciais et al.,
455 2005; Rebetez et al., 2006; Seneviratne et al., 2012). The identified drying trend in the summer season is consistent with a reported increase in agro-ecological droughts in West-Central Europe in the latest report of the Intergovernmental on Climate Change (Arias et al., 2023), and may indicate the presence of a drying trend in streamflow in this region, which was assigned low confidence at the time of the IPCC report (Seneviratne et al., 2021).

In the winter months, an increase in runoff in the Pre-Alps may be linked to an earlier onset of snowmelt (Vorkauf et al.,
460 2021). In the same region and other medium-altitude ~~regions-areas~~ such as the Jura sub-alpine mountain range, runoff is ~~lower~~ decreasing in spring. This could be related to a combination of a trend towards lower snowmelt due to less snowfall during winter (Matiu et al., 2021) and an earlier onset of snowmelt due to warmer temperatures mentioned previously. The Alps are, supposedly, similarly affected by those effects, yet the onset of thawing is delayed due to higher altitudes, and hence we see the

main contribution to negative trends in later summer. In Ticino, a strong trend towards warmer temperatures has been reported, although precipitation seems to not show significant trends (Reinhard et al., 2005). ~~We hypothesize that the~~ The negative trend in summer is ~~less related to snowmelt but rather connected to~~ likely caused by both a lack of snowmelt and an increase in evapotranspiration via warmer air temperatures, which can have a significant impact on runoff (Teuling et al., 2013; Goulden and Bales, 2014).

5.4 Potential applications

Other than catchment-level observations, the spatially and temporally complete reconstruction provides a tool for studying runoff beyond the observational horizon and also for ungauged catchments. The focus on catchments with low human impacts during model training allows the investigation of physical processes in isolation. This is an advantage for climate-focused studies, as it is challenging and often not possible to disentangle effects from human water use from physical effects associated with human-induced climate change. We encourage researchers to use the CH-RUN product for trend analysis and to understand the drivers of the simulated patterns. We further see potential in using CH-RUN as an independent benchmark dataset for hydrological models: It is challenging to understand the different sources of uncertainty during model development. Having a methodologically independent benchmark dataset can help disentangle methodological from data limitations.

With our data-driven approach, we achieve a speedup by a factor of 600 compared to PREVAH, assuming PREVAH is run parallelized across 100 central processing units (CPUs) and the CH-RUN is employed on a high-performance graphics processing unit (GPU). The reconstruction for the entire domain took approximately 20 seconds for one ensemble member on a NVIDIA A100 GPU. This speedup enables computationally cheap real-time monitoring of runoff on national scale. In addition, the model can be fed with meteorological forecasts, which would enable early warning of floods and droughts. A common use case for hydrological models is running scenarios, i.e., to simulate responses to a changing climate or to attribute runoff patterns to anthropogenic forcing. However, running scenarios with physically-based models is computationally expensive, which limits ensemble size and forecast horizon. The speedup compared to a traditional hydrological model allows running thousands of scenarios with ease. The application in early warning and running scenarios must be carefully examined and may require further calibration steps, but hold potential for understanding and mitigating climate change impacts in the near future.

5.5 Limitations

In the evaluation at the catchment level, it was observed that the CH-RUN model, although effective in general, faces challenges under certain conditions in accurately representing runoff, such as catchments with low runoff mean and variance. The model's performance was evaluated in catchments with minimal human impact, such as dam operations and surface irrigation, to reduce anthropogenic influences on the results. However, the model did not incorporate detailed land use information beyond basic surface classifications, thereby not accounting for direct human alterations in the hydrological system.

A limitation in our approach was the reliance solely on air temperature and precipitation data for long-term reconstruction, excluding other meteorological factors like ~~cloud-related effects, which could only be indirectly~~ sunshine hours, which can only be implicitly approximated by the model via the available input variables. The assumption of static variables, such as

land use and glacier coverage, being constant over time is a necessary simplification but introduces potential inaccuracies. This is particularly critical as land use can vary and glacier areas are known to decrease over time, potentially leading to biases, especially in the early stages of the reconstruction where observational data are sparse.

500 Moreover, the dataset used for training the model and the dataset for reconstruction are not entirely independent, though they are not identical. The temporal overlap of the training set within the reconstruction period was unavoidable due to data limitations. Efforts were made to mitigate the risk of overfitting by employing a distinct validation set, both spatially and temporally separated from the training data.

In runoff modeling, the quality of meteorological drivers has a large impact on model performance, and both meteorological products used here have known limitations. The TabsD product of air temperature shows a clear relationship between the error and the number of stations used for the interpolation, which results in larger errors in the 1960s and 70s most expressed in winter months and particularly in the Alps and in Ticino. The linear trend (1961-2010) of interpolated air temperature shows relatively low agreement with the observed trends (Frei, 2014). The RhiresD precipitation product is affected by two primary sources of uncertainty: The rain-gauge measurements are prone to undercatch, leading to underestimation of precipitation particularly with heavy winds and snow in general (Neff, 1977). This leads, in Switzerland, to an underestimation of about 4 % at low elevations and up to 40 % in high altitudes in winter (Sevruk, 1985). From the interpolation, there is a tendency to overestimate light and underestimate heavy precipitation (MeteoSwiss, 2021b), although these inaccuracies are reduced for areal aggregates such as the catchment averages deployed in the present study. We did not find any information on the accuracy over time, but we expect that the sparser measurement network in the 1960s and 70s leads to larger errors during this period, similar to the TabsD product. We expect that these uncertainties affect our results substantially. We acknowledge that in the early reconstruction period (1960s and 70s), where less measurement stations were available, the reconstruction may be less trustworthy. The low agreement of interpolated air temperature trends with observations could explain why both the PREVAH and CH-RUN struggle to represent extreme runoff trends. While we did not specifically investigate the representation of extreme runoff events in this study, we expect that the overestimation of low and underestimation of strong precipitation events results in a bias in runoff simulations.

510
515
520

Finally, our deep learning model heavily depends on the availability and diversity of data. Representing infrequent occurrences or events, which are less common in the data distribution, poses a significant challenge. Consequently, the model's ability to accurately depict rare and extreme hydrological events, such as sudden heavy rains leading to flash floods, is likely limited. This aspect is underscored by the inherent difficulties in modeling the "long tail" of event distribution (Zhang et al., 2023).

525

6 Conclusions

In this study, we developed a data-driven daily runoff reconstruction product for Switzerland, spanning from 1962 to 2023. Our model not only matched but also surpassed the performance of an operational hydrological model at the catchment level. This achievement is particularly noteworthy considering the reduced data requirements, a limitation necessary to achieve such

530 an extensive reconstruction period. Our model effectively captured daily runoff patterns ~~,~~ and interannual variability, and represents long-term trends decently, providing a comprehensive and satisfying depiction of runoff dynamics.

The reconstruction product revealed interesting patterns in long-term runoff trends that align with prior knowledge. Having additional reconstruction for the 1960s and 1970s, it seems that increases in the frequency, rather than in the amplitude of dry years, as well as a decrease in the frequency of wet years, is contributing towards the negative decadal ~~trend. A clear tendency~~ ~~towards drier conditions was diagnosed and~~ runoff trend. We diagnosed a trend towards lower runoff at the national scale, which was mainly linked to the summer months, where the spatial patterns of runoff indicated increasingly dry conditions particularly in mid-to-high altitudes. We encourage the in-depth investigation of the identified patterns in subsequent studies.

One of the major strengths of our approach lies in its computational efficiency, which opens up possibilities for contiguous near real-time monitoring and potentially forecasting of runoff. The reduced data demands of our model make it an invaluable tool for scenario simulation and attributing trends to anthropogenic climate change, allowing for the rapid evaluation of thousands of scenarios that were not feasible with traditional physically-based models.

Looking ahead, we believe that the current approach could be further enhanced by integrating additional data constraints or incorporating physical knowledge. Specifically, for a more accurate representation of large catchments, we see the inclusion of routing processes as a vital next step.

545 *Code and data availability.* The code is shared on GitHub and available at <https://github.com/bask0/mach-flow/>. The upscaling product (“CH-RUN”), including the input data (precipitation, temperature, and the static variables) and the catchment polygons, is available at [will be published prior to publication].

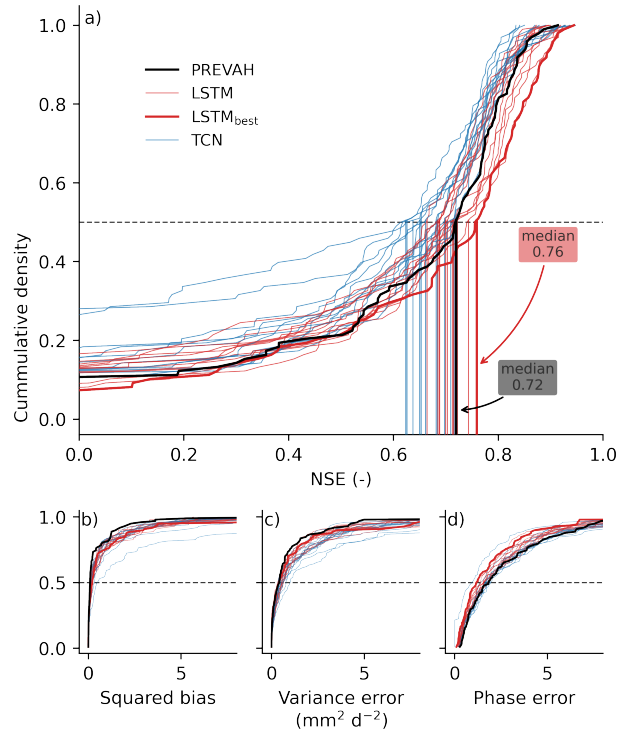


Figure 3. Model-setup impact on The catchment-level model performance and their interactions based on across the median-catchment Nash-Sutcliffe modeling efficiency (NSE), 98 catchments evaluated on the spatially and temporally independent test set that was not used for model calibration. The colors represent NSE relative to We show different versions of the respective data-driven models corresponding to model mean across setups; red represents worse, and blue represents better performance the convolution-based architectures (TCN), and red the LSTM architectures. The background gradients have been calculated using linear least square regression with the PREVAH model performance (black solid line) serves as dependent variable a benchmark. The offset lower triangular panels show results for the best-performing model (LSTM_{best}), the offset upper triangular used for the TCN model reconstruction, i.e., variable interactions, while the three panels on the diagonal show variable main effects, split to distinguish between the two models is highlighted. The x- and y-axes represent y-axis represents the setups tested in cumulative probability density, i.e., the factorial experiment. Training catchments refers to the catchments used for training: a subset fraction of 98 catchments less impacted by anthropogenic factors (C_{98}), that have given value or all catchments lower. Panel a) shows the Nash-Sutcliffe modeling efficiency (C_{267} NSE) with median values as vertical lines. Target transform is either T_{none} if the target variable was not transformed The panels b)–d) show squared bias, or T_{sqrt} for square root transform variance error, and phase error, respectively. Static variables is S_{all} if all static variables are used Note that here, S_{PCA} if they are first transformed using PCA other than for NSE in panel a), or S_{area} if only catchment-area lower values are better. The x-axes is used beyond the meteorological variable truncated.

For the LSTM architecture, using all training catchments and all static variables had a larger impact on the outcome than the square root transform of the target variable, which was negligible. The factors “training catchments” and “static variables” interacted strongly, indicating that having both more training data and more information on catchment properties contributes more to the model performance than using the factors independently. The interaction with “target transform”, in contrast, was minimal for the LSTM architectures. For the TCN models, the results look different. Using more static variables as input seems to have improved model performance, while using additional training catchments did so only marginally, and the interactions of the “training catchments” and “static variables” was less clear.

Overall, the TCN models show lower range of performance across setups than the LSTM models.

From the fusion methods introduced in Sect. 3.1, prefusion with encoding was selected most often for the LSTM architecture, while

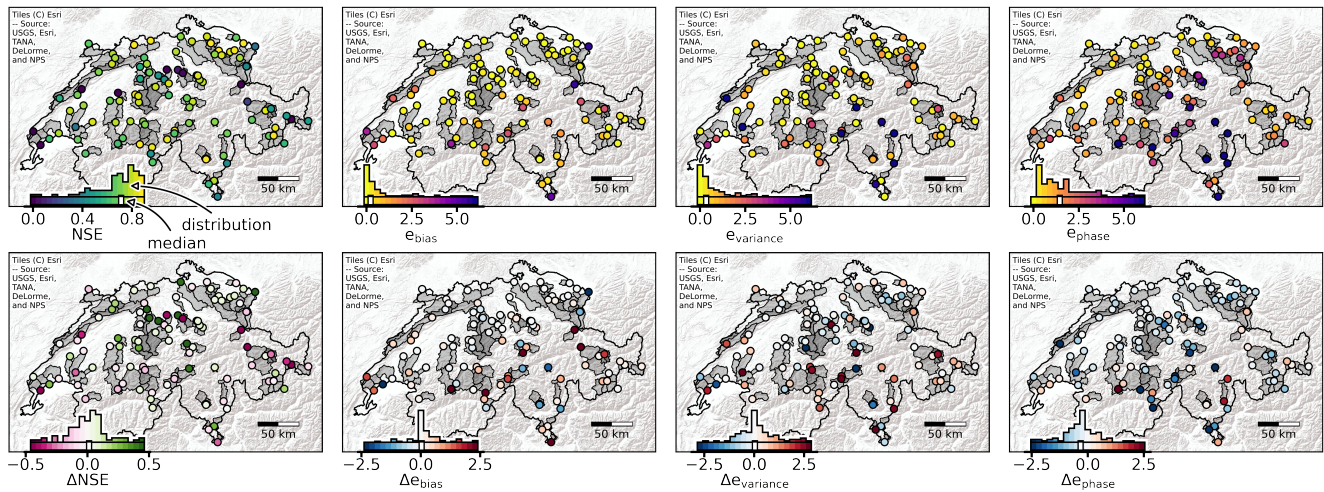


Figure 4. Spatial catchment-level performance of our best-performing model (“LSTM_{best}”) contrasted to the PREVAH hydrological model. The top row shows the performance of LSTM_{best}, with the Nash-Sutcliffe modeling efficiency (NSE) in the most-left panel, and bias (e_{bias}), variance ($e_{variance}$), and phase (e_{phase}) error, in the remaining panels. Note that in the top panel, yellowish colors indicate better performance, i.e., for NSE, a larger number is better and for the error components, lower numbers are preferred. The bottom row shows the performance difference of LSTM_{best} minus PREVAH. Here, reddish colors indicate that PREVAH performs better than LSTM_{best}, which is, for NSE, negative values, and for the error components, positive values. The inset histograms represent the distribution of catchment metrics, and the white bar indicates the median of the distribution, per panel. The evaluation is performed on the test set, but all catchments are in this set once in our cross-validation setup.

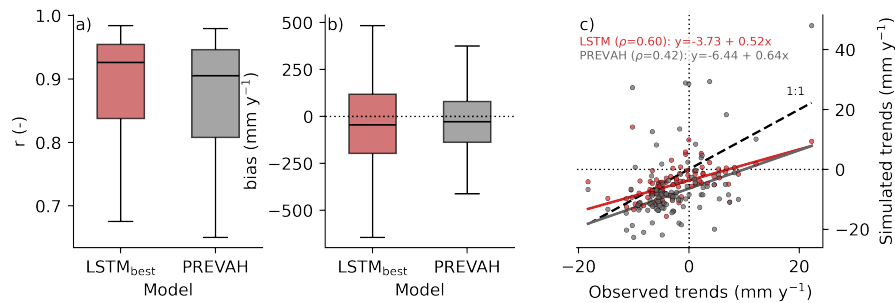


Figure 5. Catchment-level evaluation at the annual scale. a) The Pearson correlation (r) and b) bias in mm y^{-1} distribution across 98 training catchments evaluated on the test set. c) The simulated annual runoff trends compared to observations. The points represent the linear trend (found by robustified least square-squares fit) of single catchments. Note that for the trend calculation, the time range from 1995 (start of first test period) to 2020 (end of second test period) was used. The inset equation shows the linear least square fit and the corresponding rank correlations. The shaded areas represent the respective 95% confidence bands.

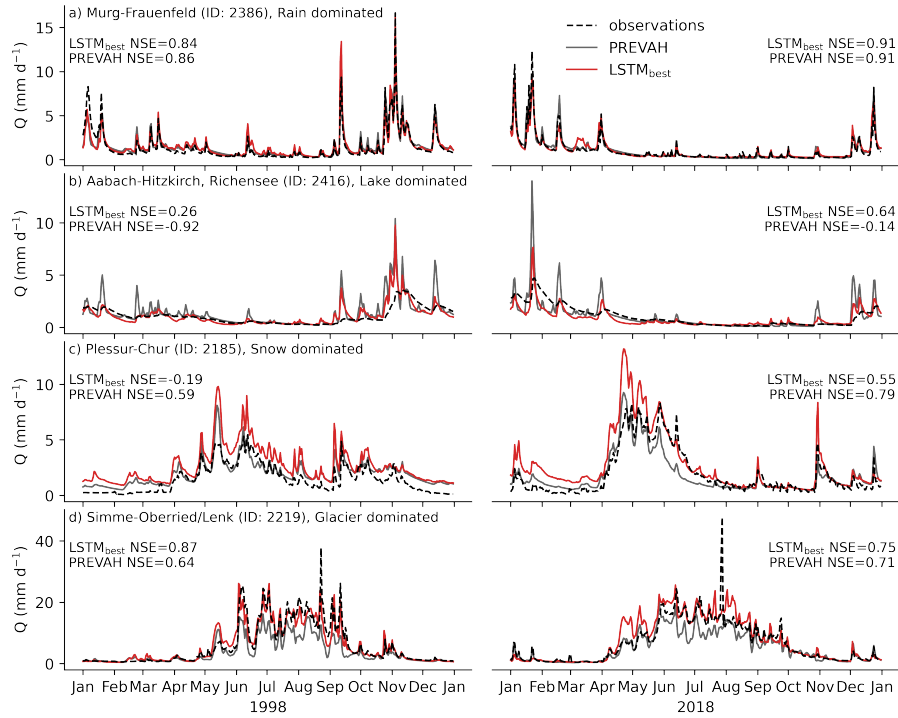


Figure 6. Daily runoff Q in mm d^{-1} for four selected catchments and two distinct years selected from the test periods. Observed (dashed black line), simulated by PREVAH (grey), and out-of-catchment prediction of the data-driven LSTM_{best} (red) are shown. The catchments were selected to represent different modeling challenges: a) rainfall, b) lake, c) snow, and d) glacier dominated. The inset NSE values represent the model performance for the selected year.

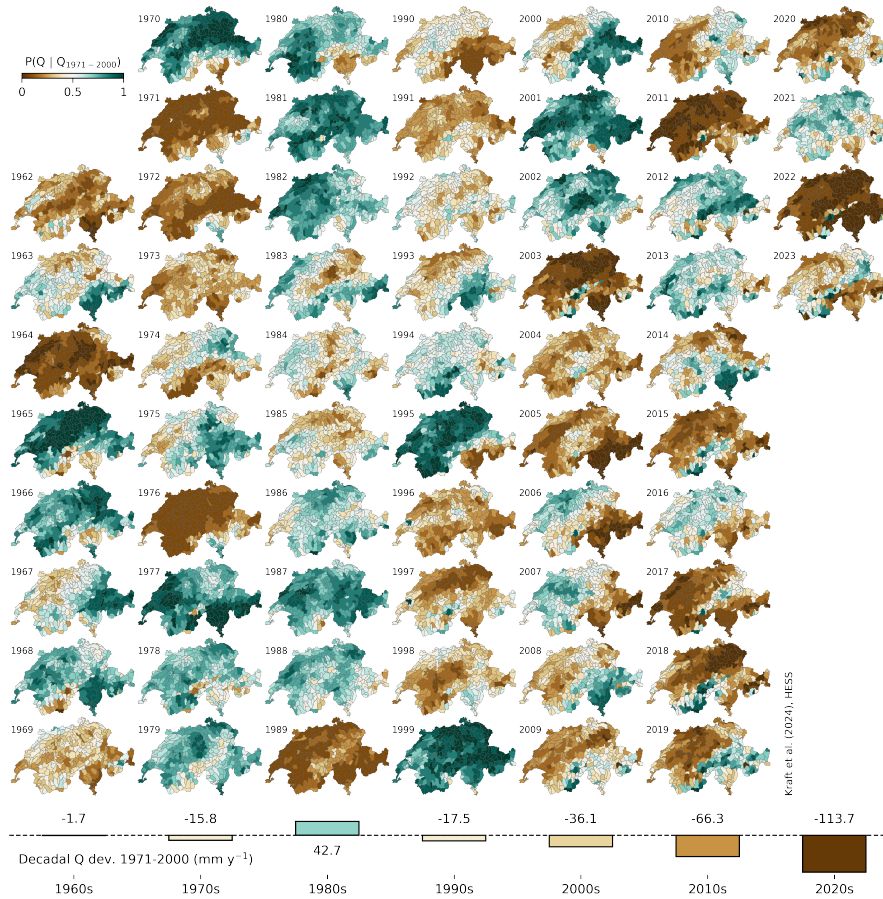


Figure 7. Spatially contiguous reconstruction of runoff from 1962 to ~~2023~~ 2023 from the CH-RUN reconstruction. The maps represent the yearly catchment-level runoff quantiles relative to the reference period (1971 to 2000) empirical distribution. The bottom bars show the decadal deviation in mm y^{-1} of the national-level runoff relative to the reference period (1971 to 2000).

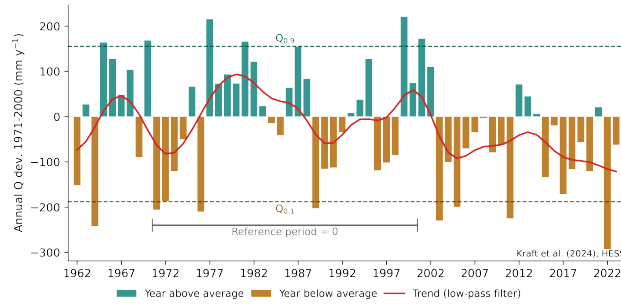


Figure 8. Annual runoff anomalies for Switzerland from 1962 to 2023 as simulated by from the LSTM (CH-RUN) reconstruction. The bars represent the CH-RUN annual deviation in mm y^{-1} of the national-level runoff relative to the reference period (1971 to 2000). The aggregation from catchment to national level was done with area-weighted mean. Positive anomalies are depicted in turquoise, negative ones in brown. The solid red line represents the trend, i.e., the low-pass filtered signal using a Gaussian filter with a standard deviation of $\sigma = 2$. The dashed lines are the 0.1 and 0.9 quantile of the reference period, respectively.

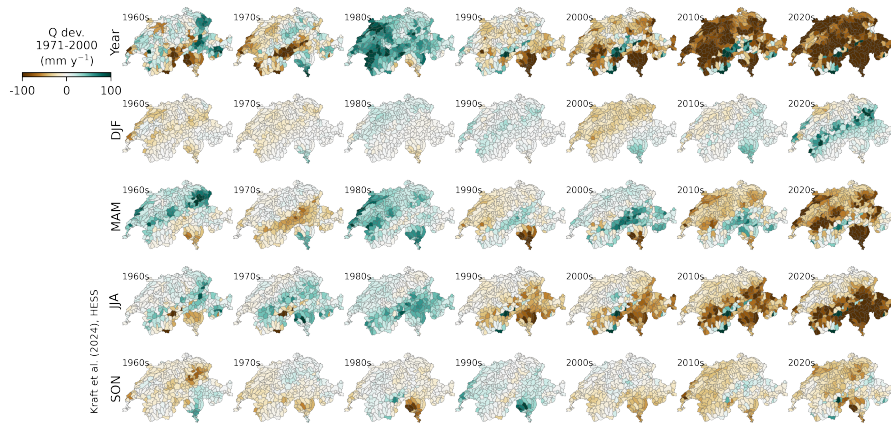


Figure 9. Decadal evolution of spatially contiguous reconstruction of runoff from 1962 to 2022 by season from the CH-RUN reconstruction. The maps represent the decadal average catchment-level runoff in mm y^{-1} relative to the reference period (1971 to 2000). From top row to bottom: Year: full year; DJF: December to February; MAM: March to May; JJA: June to August; SON: September to November.

Table A1. The search space for hyperparameter tuning. The common hyperparameters were used for both architectures, the other [ense-ones](#) are model-specific.

Name	Search space
Common parameters	
model_dim	{64, 128, 256 }
enc_dropout	{0.0, 0.2}
fusion_method	{‘pre_encoded’, ‘pre_repeated’, ‘post_repeated’ }
learning_rate	{1e-4, 1e-3, 1e-2}
weight_decay	{1e-1, 1e-2, 1e-3}
LSTM parameters	
temp_layers	{1, 2}
TCN parameters	
temp_layers	{2, 3, 4}
kernel_size	{8, 16}
temporal_dropout	{0.0, 0.2}

The `model_dim` corresponds to the model dimensionality, which is shared among all feed-forward and temporal neural networks. `enc_dropout` was used in the encoder layers prior to the temporal layer, and `fusion_method` corresponds to the approaches described in Sect. 3.1. `learning_rate` and `weight_decay` are parameters of the optimizer and control the weight update step size and regularization, respectively. For the long short-term memory (LSTM) and the temporal convolutional network (TCN), `temp_layers` defines the number of stacked temporal layers. For the latter, `kernel_size` is the width of the 1D convolution kernel applied along the time dimension, and `temporal_dropout` deactivates entire channels of input encoding, instead of randomly dropping activations.

Appendix A: Model training

A1 Hyperparameter tuning

550 The hyperparameter space searched [is](#) shown in Tab. A1. The `model_dim` denotes the model dimensionality, i.e., the size of the internal representations. The `enc_dropout` refers to dropout (random deactivation of nodes with probability p during training) applied in the encoding layers, and `fusion_method` to the method used for fusion of the temporal and static variables. For the AdamW optimizer, `learning_rate` [denotes](#) the step size, and `weight_decay` the L2 regularization. The `temp_layers` refers to the number of stacked temporal layers for both the LSTM and the TCN, and
555 `kernel_size` is the dimensionality of the 1D kernel used for convolution in the time dimension for the latter. An optional `temporal_dropout` is used for the TCN. The performance of the models and the corresponding hyperparameters are provided in Tab. A2 for the LSTMs, and Tab. A3 for the TCNs.

Rank	NSE	allbasins	sqrttrans	static	model dim	enc dropout	fusion method	temp layers	learning rate	weight decay	num params
1	0.76	True	True	all	128	0.2	pre encoded	1	0.001	0.1	169 K
2	0.74	False	True	all	256	0.2	pre encoded	2	0.001	0.01	1200 K
3	0.72	False	False	dred	128	0.2	pre encoded	2	0.001	0.1	298 K
4	0.72	True	False	all	256	0.2	pre encoded	1	0.001	0.01	668 K
7	0.71	False	False	all	128	0.2	pre encoded	2	0.01	0.1	301 K
8	0.71	True	True	dred	128	0.2	pre encoded	2	0.001	0.1	298 K
10	0.70	False	True	area	128	0.0	post repeated	2	0.001	0.1	330 K
11	0.70	True	True	area	256	0.0	post repeated	1	0.001	0.01	790 K
13	0.69	True	False	area	256	0.2	pre repeated	1	0.0001	0.01	659 K
14	0.69	False	True	dred	256	0.2	pre encoded	2	0.001	0.001	1200 K
15	0.68	False	False	area	64	0.0	post repeated	1	0.001	0.1	50 K
18	0.66	True	False	dred	128	0.2	pre encoded	2	0.01	0.1	298 K

Table A2. Hyperparameters found by tuning for the LSTM-based architectures. The rows are sorted by the catchment-level Nash-Sutcliffe modeling efficiency (NSE) in descending order, and the rank column represents the overall rank among all models. White columns denote the model setup. Yellow columns represent architecture, the magenta ones optimizer parameters, and cyan is the number of tunable parameters. [The column allbasins \(using additional catchments for training or not\), sqrttrans \(transform runoff with square root or not\), and static \(use all static variable, a dimensionality-reduced version, or none\) refer to the factorial experiments described in Sect. 3.5.](#)

Rank	NSE	allbasins	sqrttrans	static	model dim	enc dropout	fusion method	temp layers	kernel size	learning rate	weight decay	num params
5	0.72	True	False	dred	128	0.0	post repeated	3	16	0.0001	0.001	1600 K
6	0.72	False	True	dred	128	0.0	post repeated	4	16	0.0001	0.001	2200 K
9	0.71	True	True	all	256	0.0	post repeated	4	8	0.0001	0.1	4500 K
12	0.70	True	True	dred	128	0.0	post repeated	4	16	0.0001	0.001	2200 K
16	0.68	False	True	area	64	0.0	post repeated	4	16	0.001	0.1	322 K
17	0.68	True	False	area	128	0.2	pre repeated	3	16	0.0001	0.1	1600 K
19	0.66	False	False	area	128	0.2	post repeated	4	8	0.001	0.1	1100 K
20	0.65	True	True	area	128	0.0	post repeated	4	16	0.0001	0.001	2200 K
21	0.65	False	True	all	256	0.2	post repeated	4	16	0.0001	0.1	8700 K
22	0.64	False	False	all	256	0.2	post repeated	4	8	0.001	0.01	4500 K
23	0.63	False	False	dred	64	0.0	pre repeated	4	8	0.001	0.01	272 K
24	0.62	True	False	all	256	0.2	pre encoded	4	8	0.0001	0.1	4300 K

Table A3. Hyperparameters found by tuning for the TCN-based architectures. The rows are sorted by the catchment-level Nash-Sutcliffe modeling efficiency (NSE) in descending order, and the rank column represents the overall rank among all models. White columns denote the model setup. Yellow columns represent architecture, the magenta ones optimizer parameters, and cyan is the number of tunable parameters. [The column allbasins \(using additional catchments for training or not\), sqrttrans \(transform runoff with square root or not\), and static \(use all static variable, a dimensionality-reduced version, or none\) refer to the factorial experiments described in Sect. 3.5.](#)

560 From the fusion methods introduced in Sect. 3.1, [prefusion with encoding was selected most often for the LSTM architecture, while postfusion was more commonly selected for the TCN \(A, Tab. A2 & A3\). Note that the fusion was part of the hyperparameter tuning, and only the best approach is used to make the final predictions. For both architectures, prefusion with encoding was commonly selected if all static variables were used as input. Interestingly, as seen in the Tab. A2 & A3, the number of tunable parameters, an outcome of the hyperparameter tuning process, was larger by a factor of five for the TCN architectures \(2.8 million in average\) compared to the LSTMs \(0.52 million in average\).](#)

A2 [Comparison of model setups](#)

565 [Here, we evaluate the factorial experiment outlined in Sect. 3.5. In Fig. A1, the diagonal shows how the model setups impacts the median NSE across catchments, and the offset triangular shows the interactions of the factors.](#)

[For the LSTM architecture, using all training catchments and all static variables had a larger impact on the outcome than the square root transform of the target variable, which was negligible. The factors “training catchments” and “static variables” interacted strongly, indicating that having both more training data and more information on catchment properties contributes](#)

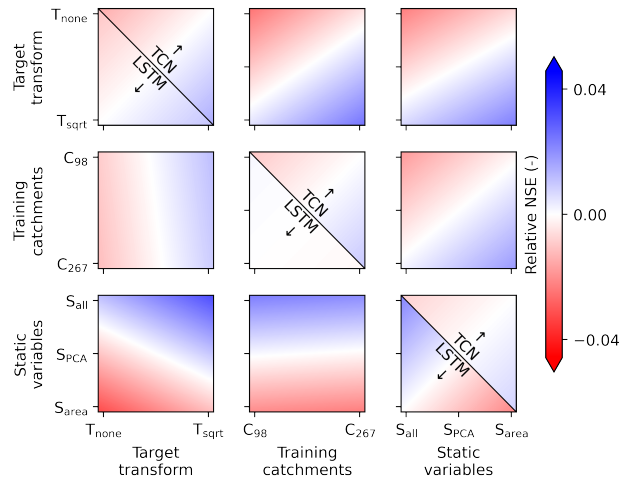


Figure A1. Model setup impact on performance and their interactions based on the median catchment Nash-Sutcliffe modeling efficiency (NSE), evaluated on the spatially and temporally independent test set. The colors represent NSE relative to the respective model mean across setups; red represents worse, and blue represents better performance. The background gradients have been calculated using linear least square regression with the model performance as dependent variable. The offset lower triangular panels show results for the LSTM, the offset upper triangular for the TCN model, i.e., variable interactions, while the three panels on the diagonal show variable main effects, split to distinguish between the two models. The x and y axes represent the setups tested in the factorial experiment. *Training catchments* refers to the catchments used for training: a subset of 98 catchments less impacted by anthropogenic factors (C_{98}), or all catchments (C_{267}). *Target transform* is either T_{none} if the target variable was not transformed, or T_{sqrt} for square root transform. *Static variables* is S_{all} if all static variables are used, S_{PCA} if they are first transformed using PCA, or S_{area} if only catchment area is used beyond the meteorological variables.

570 more to the model performance than using the factors independently. The interaction with “target transform”, in contrast, was minimal for the LSTM architectures. For the TCN models, the results look different. Using more static variables as input seems to have improved model performance, while using additional training catchments did so only marginally, and the interactions of the “training catchments” and “static variables” was less clear. Overall, the TCN models show lower range of performance across setups than the LSTM models.

575 *Author contributions.* The study was planned and designed by BK, LG, MS, and WA. Data was processed by MS and WA. MZ provided the PREVAH benchmark. The data pipeline and model implementation, and visualization of results were conducted by BK. BK took the lead in the preparation of the manuscript, but all authors contributed.

Competing interests. The contact author has declared that none of the authors has any competing interests.

Acknowledgements. We acknowledge the funding from the Swiss Data Science Center project C20-02 ~~Machine learning for Swiss (CH) river flow estimation (MACH-Flow)~~ Machine learning for Swiss (CH) river flow estimation (MACH-Flow). We would like to express our gratitude to the anonymous reviewer #1 and Ross Woods, and Editor Nunzio Romano for their thoughtful comments, constructive feedback, and guidance throughout the peer-review process, which significantly improved the quality of this manuscript.

References

- Addor, N. and Melsen, L. A.: Legacy, Rather Than Adequacy, Drives the Selection of Hydrological Models, *Water Resources Research*, 55, 378–390, <https://doi.org/10.1029/2018WR022958>, 2019.
- Addor, N., Newman, A. J., Mizukami, N., and Clark, M. P.: The CAMELS Data Set: Catchment Attributes and Meteorology for Large-Sample Studies, *Hydrology and Earth System Sciences*, 21, 5293–5313, <https://doi.org/10.5194/hess-21-5293-2017>, 2017.
- Akiba, T., Sano, S., Yanase, T., Ohta, T., and Koyama, M.: Optuna: A Next-generation Hyperparameter Optimization Framework, in: Proceedings of the 25th ACM SIGKDD International Conference on Knowledge Discovery & Data Mining, KDD '19, pp. 2623–2631, Association for Computing Machinery, New York, NY, USA, ISBN 978-1-4503-6201-6, <https://doi.org/10.1145/3292500.3330701>, 2019.
- Amari, S.-i.: Backpropagation and Stochastic Gradient Descent Method, *Neurocomputing*, 5, 185–196, [https://doi.org/10.1016/0925-2312\(93\)90006-O](https://doi.org/10.1016/0925-2312(93)90006-O), 1993.
- Arias, P. A., Bellouin, N., Coppola, E., Jones, R. G., Krinner, G., Marotzke, J., Naik, V., Palmer, M. D., Plattner, G.-K., and Rogelj, J.: Intergovernmental Panel on Climate Change (IPCC). Technical Summary, in: *Climate Change 2021: The Physical Science Basis. Contribution of Working Group I to the Sixth Assessment Report of the Intergovernmental Panel on Climate Change*, pp. 35–144, Cambridge University Press, 2023.
- Bai, S., Kolter, J. Z., and Koltun, V.: An Empirical Evaluation of Generic Convolutional and Recurrent Networks for Sequence Modeling, <https://doi.org/10.48550/arXiv.1803.01271>, 2018.
- Baltensweiler, A., Walthert, L., Zimmermann, S., and Nussbaum, M.: Hochauflösende Bodenkarten Für Den Schweizer Wald, *Schweizerische Zeitschrift für Forstwesen*, 173, 288–291, <https://doi.org/10.3188/szf.2022.0288>, 2022.
- Beck, H. E., van Dijk, A. I. J. M., de Roo, A., Miralles, D. G., McVicar, T. R., Schellekens, J., and Bruijnzeel, L. A.: Global-Scale Regionalization of Hydrologic Model Parameters, *Water Resources Research*, 52, 3599–3622, <https://doi.org/10.1002/2015WR018247>, 2016.
- Bergstra, J., Bardenet, R., Bengio, Y., and Kégl, B.: Algorithms for Hyper-Parameter Optimization, in: *Advances in Neural Information Processing Systems*, vol. 24, Curran Associates, Inc., 2011.
- Bindas, T., Tsai, W.-P., Liu, J., Rahmani, F., Feng, D., Bian, Y., Lawson, K., and Shen, C.: Improving River Routing Using a Differentiable Muskingum-Cunge Model and Physics-Informed Machine Learning, *Water Resources Research*, 60, e2023WR035337, <https://doi.org/10.1029/2023WR035337>, 2024.
- Bogner, K., Chang, A. Y.-Y., Bernhard, L., Zappa, M., Monhart, S., and Spirig, C.: Tercile Forecasts for Extending the Horizon of Skillful Hydrological Predictions, *Journal of Hydrometeorology*, 23, 521–539, <https://doi.org/10.1175/JHM-D-21-0020.1>, 2022.
- Brunner, M. I., Björnson Gurung, A., Zappa, M., Zekollari, H., Farinotti, D., and Stähli, M.: Present and Future Water Scarcity in Switzerland: Potential for Alleviation through Reservoirs and Lakes, *Science of The Total Environment*, 666, 1033–1047, <https://doi.org/10.1016/j.scitotenv.2019.02.169>, 2019a.
- Brunner, M. I., Farinotti, D., Zekollari, H., Huss, M., and Zappa, M.: Future Shifts in Extreme Flow Regimes in Alpine Regions, *Hydrology and Earth System Sciences*, 23, 4471–4489, <https://doi.org/10.5194/hess-23-4471-2019>, 2019b.
- Brunner, M. I., Liechti, K., and Zappa, M.: Extremeness of Recent Drought Events in Switzerland: Dependence on Variable and Return Period Choice, *Natural Hazards and Earth System Sciences*, 19, 2311–2323, <https://doi.org/10.5194/nhess-19-2311-2019>, 2019c.
- Brunner, M. I., Zappa, M., and Stähli, M.: Scale Matters: Effects of Temporal and Spatial Data Resolution on Water Scarcity Assessments, *Advances in Water Resources*, 123, 134–144, <https://doi.org/10.1016/j.advwatres.2018.11.013>, 2019d.

- Camps-Valls, G., Tuia, D., Zhu, X. X., and Reichstein, M.: Deep Learning for the Earth Sciences: A Comprehensive Approach to Remote Sensing, Climate Science and Geosciences, Wiley, Hoboken, NJ, 1st edition edn., ISBN 978-1-119-64614-3, 2021.
- Catling, F. J. R. and Wolff, A. H.: Temporal Convolutional Networks Allow Early Prediction of Events in Critical Care, *Journal of the American Medical Informatics Association*, 27, 355–365, <https://doi.org/10.1093/jamia/ocz205>, 2020.
- Ciais, P., Reichstein, M., Viovy, N., Granier, A., Ogée, J., Allard, V., Aubinet, M., Buchmann, N., Bernhofer, C., Carrara, A., Chevallier, F., De Noblet, N., Friend, A. D., Friedlingstein, P., Grünwald, T., Heinesch, B., Keronen, P., Knohl, A., Krinner, G., Loustau, D., Manca, G., Matteucci, G., Miglietta, F., Ourcival, J. M., Papale, D., Pilegaard, K., Rambal, S., Seufert, G., Soussana, J. F., Sanz, M. J., Schulze, E. D., Vesala, T., and Valentini, R.: Europe-Wide Reduction in Primary Productivity Caused by the Heat and Drought in 2003, *Nature*, 437, 529–533, <https://doi.org/10.1038/nature03972>, 2005.
- Daw, A., Karpatne, A., Watkins, W., Read, J., and Kumar, V.: Physics-Guided Neural Networks (PGNN): An Application in Lake Temperature Modeling, <https://doi.org/10.48550/arXiv.1710.11431>, 2021.
- Do, H. X., Gudmundsson, L., Leonard, M., and Westra, S.: The Global Streamflow Indices and Metadata Archive (GSIM) – Part 1: The Production of a Daily Streamflow Archive and Metadata, *Earth System Science Data*, 10, 765–785, <https://doi.org/10.5194/essd-10-765-2018>, 2018.
- Do Nascimento, T. V. M., Rudlang, J., Höge, M., Van Der Ent, R., Chappon, M., Seibert, J., Hrachowitz, M., and Fenicia, F.: EStreams: An Integrated Dataset and Catalogue of Streamflow, Hydro-Climatic Variables and Landscape Descriptors for Europe, Preprint, *Earth Sciences*, <https://doi.org/10.31223/X5M39F>, 2024.
- FOEN: Hydrological Data Service for Watercourses and Lakes, <https://www.bafu.admin.ch/bafu/en/home/themen/thema-wasser/wasser-daten-indikatoren-und-karten/wasser-messwerte-und-statistik/messwerte-zum-thema-wasser-beziehen/datenservice-hydrologie-fuer-fliessgewaesser-und-seen.html>, last access: 1 April 2024, 2024.
- Frei, C.: Interpolation of Temperature in a Mountainous Region Using Nonlinear Profiles and Non-Euclidean Distances, *International Journal of Climatology*, 34, 1585–1605, <https://doi.org/10.1002/joc.3786>, 2014.
- Gauch, M., Kratzert, F., Klotz, D., Nearing, G., Lin, J., and Hochreiter, S.: Rainfall–Runoff Prediction at Multiple Timescales with a Single Long Short-Term Memory Network, *Hydrology and Earth System Sciences*, 25, 2045–2062, <https://doi.org/10.5194/hess-25-2045-2021>, 2021a.
- Gauch, M., Mai, J., and Lin, J.: The Proper Care and Feeding of CAMELS: How Limited Training Data Affects Streamflow Prediction, *Environmental Modelling & Software*, 135, 104926, <https://doi.org/10.1016/j.envsoft.2020.104926>, 2021b.
- Ghiggi, G., Humphrey, V., Seneviratne, S. I., and Gudmundsson, L.: GRUN: An Observation-Based Global Gridded Runoff Dataset from 1902 to 2014, *Earth System Science Data*, 11, 1655–1674, <https://doi.org/10.5194/essd-11-1655-2019>, 2019.
- Ghiggi, G., Humphrey, V., Seneviratne, S. I., and Gudmundsson, L.: G-RUN ENSEMBLE: A Multi-Forcing Observation-Based Global Runoff Reanalysis, *Water Resources Research*, 57, e2020WR028787, <https://doi.org/10.1029/2020WR028787>, 2021.
- Goulden, M. L. and Bales, R. C.: Mountain Runoff Vulnerability to Increased Evapotranspiration with Vegetation Expansion, *Proceedings of the National Academy of Sciences*, 111, 14071–14075, <https://doi.org/10.1073/pnas.1319316111>, 2014.
- Gudmundsson, L. and Seneviratne, S. I.: Towards Observation-Based Gridded Runoff Estimates for Europe, *Hydrology and Earth System Sciences*, 19, 2859–2879, <https://doi.org/10.5194/hess-19-2859-2015>, 2015.
- Gudmundsson, L., Do, H. X., Leonard, M., and Westra, S.: The Global Streamflow Indices and Metadata Archive (GSIM) – Part 2: Quality Control, Time-Series Indices and Homogeneity Assessment, *Earth System Science Data*, 10, 787–804, <https://doi.org/10.5194/essd-10-787-2018>, 2018.

- Gupta, H. V., Kling, H., Yilmaz, K. K., and Martinez, G. F.: Decomposition of the Mean Squared Error and NSE Performance Criteria: Implications for Improving Hydrological Modelling, *Journal of Hydrology*, 377, 80–91, <https://doi.org/10.1016/j.jhydrol.2009.08.003>, 2009.
- 660 Hanel, M., Rakovec, O., Markonis, Y., Máca, P., Samaniego, L., Kyselý, J., and Kumar, R.: Revisiting the Recent European Droughts from a Long-Term Perspective, *Scientific Reports*, 8, 9499, <https://doi.org/10.1038/s41598-018-27464-4>, 2018.
- Hengl, T., de Jesus, J. M., Heuvelink, G. B. M., Gonzalez, M. R., Kilibarda, M., Blagotić, A., Shangguan, W., Wright, M. N., Geng, X., Bauer-Marschallinger, B., Guevara, M. A., Vargas, R., MacMillan, R. A., Batjes, N. H., Leenaars, J. G. B., Ribeiro, E., Wheeler, I., Mantel, S., and Kempen, B.: SoilGrids250m: Global Gridded Soil Information Based on Machine Learning, *PLOS ONE*, 12, e0169748, 665 <https://doi.org/10.1371/journal.pone.0169748>, 2017.
- Henne, P. D., Bigalke, M., Büntgen, U., Colombaroli, D., Conedera, M., Feller, U., Frank, D., Fuhrer, J., Grosjean, M., Heiri, O., Luterbacher, J., Mestrot, A., Rigling, A., Rössler, O., Rohr, C., Rutishauser, T., Schwikowski, M., Stampfli, A., Szidat, S., Theurillat, J.-P., Weingartner, R., Wilcke, W., and Tinner, W.: An Empirical Perspective for Understanding Climate Change Impacts in Switzerland, *Regional Environmental Change*, 18, 205–221, <https://doi.org/10.1007/s10113-017-1182-9>, 2018.
- 670 Hochreiter, S. and Schmidhuber, J.: Long Short-Term Memory, *Neural Computation*, 9, 1735–1780, <https://doi.org/10.1162/neco.1997.9.8.1735>, 1997.
- Höge, M., Scheidegger, A., Baity-Jesi, M., Albert, C., and Fenicia, F.: Improving Hydrologic Models for Predictions and Process Understanding Using Neural ODEs, *Hydrology and Earth System Sciences*, 26, 5085–5102, <https://doi.org/10.5194/hess-26-5085-2022>, 2022.
- Höge, M., Kauzlaric, M., Siber, R., Schönenberger, U., Horton, P., Schwanbeck, J., Floriancic, M. G., Viviroli, D., Wilhelm, S., Sikorska-Senoner, A. E., Addor, N., Brunner, M., Pool, S., Zappa, M., and Fenicia, F.: CAMELS-CH: Hydro-Meteorological Time Series and Landscape Attributes for 331 Catchments in Hydrologic Switzerland, *Earth System Science Data*, 15, 5755–5784, <https://doi.org/10.5194/essd-15-5755-2023>, 2023.
- Hohmann, C., Kirchengast, G., and Birk, S.: Alpine Foreland Running Drier? Sensitivity of a Drought Vulnerable Catchment to Changes in Climate, Land Use, and Water Management, *Climatic Change*, 147, 179–193, <https://doi.org/10.1007/s10584-017-2121-y>, 2018.
- 680 Horton, P., Schaeffli, B., and Kauzlaric, M.: Why Do We Have so Many Different Hydrological Models? A Review Based on the Case of Switzerland, *WIREs Water*, 9, e1574, <https://doi.org/10.1002/wat2.1574>, 2022.
- Huber, P. J. and Ronchetti, E. M.: *Robust Statistics*, Wiley Series in Probability and Statistics, Wiley, 1 edn., ISBN 978-0-470-12990-6 978-0-470-43469-7, <https://doi.org/10.1002/9780470434697>, 2009.
- Kebede Mengistie, G., Demissie Wondimagegnehu, K., Walker, D. W., and Tamiru Haile, A.: Value of Quality Controlled Citizen Science Data for Rainfall-Runoff Characterization in a Rapidly Urbanizing Catchment, *Journal of Hydrology*, 629, 130639, 685 <https://doi.org/10.1016/j.jhydrol.2024.130639>, 2024.
- Kobayashi, K. and Salam, M. U.: Comparing Simulated and Measured Values Using Mean Squared Deviation and Its Components, *Agronomy Journal*, 92, 345–352, <https://doi.org/10.2134/agronj2000.922345x>, 2000.
- Köplin, N., Viviroli, D., Schädler, B., and Weingartner, R.: How Does Climate Change Affect Mesoscale Catchments in Switzerland? – a 690 Framework for a Comprehensive Assessment, *Advances in Geosciences*, 27, 111–119, <https://doi.org/10.5194/adgeo-27-111-2010>, 2010.
- Kraft, B., Jung, M., Körner, M., Requena Mesa, C., Cortés, J., and Reichstein, M.: Identifying Dynamic Memory Effects on Vegetation State Using Recurrent Neural Networks, *Frontiers in Big Data*, 2, 2019.
- Kraft, B., Jung, M., Körner, M., and Reichstein, M.: HYBRID MODELING: FUSION OF A DEEP LEARNING APPROACH AND A PHYSICS-BASED MODEL FOR GLOBAL HYDROLOGICAL MODELING, *The International Archives of the Photogrammetry, Re-*

- 695 mote Sensing and Spatial Information Sciences, XLIII-B2-2020, 1537–1544, <https://doi.org/10.5194/isprs-archives-XLIII-B2-2020-1537-2020>, 2020.
- Kraft, B., Besnard, S., and Koirala, S.: Emulating Ecological Memory with Recurrent Neural Networks, in: Deep Learning for the Earth Sciences, chap. 18, pp. 269–281, John Wiley & Sons, Ltd, ISBN 978-1-119-64618-1, <https://doi.org/10.1002/9781119646181.ch18>, 2021.
- Kraft, B., Jung, M., Körner, M., Koirala, S., and Reichstein, M.: Towards Hybrid Modeling of the Global Hydrological Cycle, Hydrology and Earth System Sciences, 26, 1579–1614, <https://doi.org/10.5194/hess-26-1579-2022>, 2022.
- 700 Kratzert, F., Klotz, D., Brenner, C., Schulz, K., and Herrnegger, M.: Rainfall–Runoff Modelling Using Long Short-Term Memory (LSTM) Networks, Hydrology and Earth System Sciences, 22, 6005–6022, <https://doi.org/10.5194/hess-22-6005-2018>, 2018.
- Kratzert, F., Klotz, D., Shalev, G., Klambauer, G., Hochreiter, S., and Nearing, G.: Towards Learning Universal, Regional, and Local Hydrological Behaviors via Machine Learning Applied to Large-Sample Datasets, Hydrology and Earth System Sciences, 23, 5089–5110, <https://doi.org/10.5194/hess-23-5089-2019>, 2019.
- 705 Kratzert, F., Nearing, G., Addor, N., Erickson, T., Gauch, M., Gilon, O., Gudmundsson, L., Hassidim, A., Klotz, D., Nevo, S., Shalev, G., and Matias, Y.: Caravan - A Global Community Dataset for Large-Sample Hydrology, Scientific Data, 10, 61, <https://doi.org/10.1038/s41597-023-01975-w>, 2023.
- Kratzert, F., Gauch, M., Klotz, D., and Nearing, G.: HESS Opinions: Never Train a Long Short-Term Memory (LSTM) Network on a Single Basin, Hydrology and Earth System Sciences, 28, 4187–4201, <https://doi.org/10.5194/hess-28-4187-2024>, 2024.
- 710 Laghari, A. N., Soomro, M. A., Siyal, Z. A., Sandilo, S. H., and Soomro, T. A.: Water Availability in Snow Dominated Regions under Projected Climatic Variability: A Case Study of Alpine Catchment, Austria, Engineering, Technology & Applied Science Research, 8, 2704–2708, <https://doi.org/10.48084/etasr.1831>, 2018.
- Lees, T., Buechel, M., Anderson, B., Slater, L., Reece, S., Coxon, G., and Dadson, S. J.: Benchmarking Data-Driven Rainfall–Runoff Models in Great Britain: A Comparison of Long Short-Term Memory (LSTM)-Based Models with Four Lumped Conceptual Models, Hydrology and Earth System Sciences, 25, 5517–5534, <https://doi.org/10.5194/hess-25-5517-2021>, 2021.
- 715 Lees, T., Reece, S., Kratzert, F., Klotz, D., Gauch, M., De Bruijn, J., Kumar Sahu, R., Greve, P., Slater, L., and Dadson, S. J.: Hydrological Concept Formation inside Long Short-Term Memory (LSTM) Networks, Hydrology and Earth System Sciences, 26, 3079–3101, <https://doi.org/10.5194/hess-26-3079-2022>, 2022.
- 720 Li, L., Jamieson, K., DeSalvo, G., Rostamizadeh, A., and Talwalkar, A.: Hyperband: A Novel Bandit-Based Approach to Hyperparameter Optimization, Journal of Machine Learning Research, 18, 1–52, 2018.
- Lim, B., Arık, S. Ö., Loeff, N., and Pfister, T.: Temporal Fusion Transformers for Interpretable Multi-Horizon Time Series Forecasting, International Journal of Forecasting, 37, 1748–1764, <https://doi.org/10.1016/j.ijforecast.2021.03.012>, 2021.
- Linsbauer, A., Huss, M., Hodel, E., Bauder, A., Fischer, M., Weidmann, Y., Bärtschi, H., and Schmassmann, E.: The New Swiss Glacier Inventory SGI2016: From a Topographical to a Glaciological Dataset, Frontiers in Earth Science, 9, <https://doi.org/10.3389/feart.2021.704189>, 2021.
- 725 Loshchilov, I. and Hutter, F.: Decoupled Weight Decay Regularization, <https://doi.org/10.48550/arXiv.1711.05101>, 2019.
- Matiu, M., Crespi, A., Bertoldi, G., Carmagnola, C. M., Marty, C., Morin, S., Schöner, W., Cat Berro, D., Chiozna, G., De Gregorio, L., Kotlarski, S., Majone, B., Resch, G., Terzago, S., Valt, M., Beozzo, W., Cianfarra, P., Gouttevin, I., Marcolini, G., Notarnicola, C., Petitta, M., Scherrer, S. C., Strasser, U., Winkler, M., Zebisch, M., Cicogna, A., Cremonini, R., Debernardi, A., Faletto, M., Gaddo, M., Giovannini, L., Mercalli, L., Soubeyroux, J.-M., Sušnik, A., Trenti, A., Urbani, S., and Weilguni, V.: Observed Snow Depth Trends in the European Alps: 1971 to 2019, The Cryosphere, 15, 1343–1382, <https://doi.org/10.5194/tc-15-1343-2021>, 2021.

- MeteoSwiss: Daily Mean, Minimum and Maximum Temperature: TabsD, TminD, TmaxD, https://www.meteoschweiz.admin.ch/dam/jcr:818a4d17-cb0c-4e8b-92c6-1a1bdf5348b7/ProdDoc_TabsD.pdf, last access: 1 April 2024, 2021a.
- 735 MeteoSwiss: Daily Precipitation (Final Analysis): RhiresD, https://www.meteoschweiz.admin.ch/dam/jcr:4f51f0f1-0fe3-48b5-9de0-15666327e63c/ProdDoc_RhiresD.pdf, last access: 1 April 2024, 2021b.
- Muelchi, R., Rössler, O., Schwanbeck, J., Weingartner, R., and Martius, O.: An Ensemble of Daily Simulated Runoff Data (1981–2099) under Climate Change Conditions for 93 Catchments in Switzerland (Hydro-CH2018-Runoff Ensemble), *Geoscience Data Journal*, 9, 46–57, <https://doi.org/10.1002/gdj3.117>, 2022.
- 740 Nardi, F., Cudennec, C., Abrate, T., Allouch, C., Annis, A., Assumpção, T., Aubert, A. H., Bérod, D., Braccini, A. M., Buytaert, W., Dasgupta, A., Hannah, D. M., Mazzoleni, M., Polo, M. J., Sæbø, Ø., Seibert, J., Tauro, F., Teichert, F., Teutonico, R., Uhlenbrook, S., Wahrmann Vargas, C., and Grimaldi, S.: Citizens AND HYdrology (CANDHY): Conceptualizing a Transdisciplinary Framework for Citizen Science Addressing Hydrological Challenges, *Hydrological Sciences Journal*, 67, 2534–2551, <https://doi.org/10.1080/02626667.2020.1849707>, 2022.
- 745 Nash, J. E. and Sutcliffe, J. V.: River Flow Forecasting through Conceptual Models Part I — A Discussion of Principles, *Journal of Hydrology*, 10, 282–290, [https://doi.org/10.1016/0022-1694\(70\)90255-6](https://doi.org/10.1016/0022-1694(70)90255-6), 1970.
- Nasreen, S., Součková, M., Vargas Godoy, M. R., Singh, U., Markonis, Y., Kumar, R., Rakovec, O., and Hanel, M.: A 500-Year Annual Runoff Reconstruction for 14 Selected European Catchments, *Earth System Science Data*, 14, 4035–4056, <https://doi.org/10.5194/essd-14-4035-2022>, 2022.
- 750 Nearing, G. S., Kratzert, F., Sampson, A. K., Pelissier, C. S., Klotz, D., Frame, J. M., Prieto, C., and Gupta, H. V.: What Role Does Hydrological Science Play in the Age of Machine Learning?, *Water Resources Research*, 57, e2020WR028091, <https://doi.org/10.1029/2020WR028091>, 2021.
- Neff, E. L.: How Much Rain Does a Rain Gage Gage?, *Journal of Hydrology*, 35, 213–220, [https://doi.org/10.1016/0022-1694\(77\)90001-4](https://doi.org/10.1016/0022-1694(77)90001-4), 1977.
- 755 Orth, R. and Destouni, G.: Drought Reduces Blue-Water Fluxes More Strongly than Green-Water Fluxes in Europe, *Nature Communications*, 9, 3602, <https://doi.org/10.1038/s41467-018-06013-7>, 2018.
- Otero, N., Horton, P., Martius, O., Allen, S., Zappa, M., Wechsler, T., and Schaeffli, B.: Impacts of Hot-Dry Conditions on Hydropower Production in Switzerland, *Environmental Research Letters*, 18, 064038, <https://doi.org/10.1088/1748-9326/acd8d7>, 2023.
- Pan, S. J. and Yang, Q.: A Survey on Transfer Learning, *IEEE Transactions on Knowledge and Data Engineering*, 22, 1345–1359, <https://doi.org/10.1109/TKDE.2009.191>, 2010.
- 760 Poggio, L., de Sousa, L. M., Batjes, N. H., Heuvelink, G. B. M., Kempen, B., Ribeiro, E., and Rossiter, D.: SoilGrids 2.0: Producing Soil Information for the Globe with Quantified Spatial Uncertainty, *SOIL*, 7, 217–240, <https://doi.org/10.5194/soil-7-217-2021>, 2021.
- Price, B., Huber, N., Nussbaumer, A., and Ginzler, C.: The Habitat Map of Switzerland: A Remote Sensing, Composite Approach for a High Spatial and Thematic Resolution Product, *Remote Sensing*, 15, 643, <https://doi.org/10.3390/rs15030643>, 2023.
- 765 Rebetez, M., Mayer, H., Dupont, O., Schindler, D., Gartner, K., Kropp, J. P., and Menzel, A.: Heat and Drought 2003 in Europe: A Climate Synthesis, *Annals of Forest Science*, 63, 569–577, <https://doi.org/10.1051/forest:2006043>, 2006.
- Reichstein, M., Besnard, S., Carvalhais, N., Gans, F., Jung, M., Kraft, B., and Mahecha, M.: Modelling Landsurface Time-Series with Recurrent Neural Nets, in: *IGARSS 2018 - 2018 IEEE International Geoscience and Remote Sensing Symposium*, pp. 7640–7643, ISSN 2153-7003, <https://doi.org/10.1109/IGARSS.2018.8518007>, 2018.

- 770 Reichstein, M., Camps-Valls, G., Stevens, B., Jung, M., Denzler, J., Carvalhais, N., and Prabhat: Deep Learning and Process Understanding for Data-Driven Earth System Science, *Nature*, 566, 195–204, <https://doi.org/10.1038/s41586-019-0912-1>, 2019.
- Reinhard, M., Rebetez, M., and Schlaepfer, R.: Recent Climate Change: Rethinking Drought in the Context of Forest Fire Research in Ticino, South of Switzerland, *Theoretical and Applied Climatology*, 82, 17–25, <https://doi.org/10.1007/s00704-005-0123-6>, 2005.
- Sadler, J. M., Appling, A. P., Read, J. S., Oliver, S. K., Jia, X., Zwart, J. A., and Kumar, V.: Multi-Task Deep Learning of Daily Streamflow
775 and Water Temperature, *Water Resources Research*, 58, e2021WR030138, <https://doi.org/10.1029/2021WR030138>, 2022.
- Schumacher, D. L., Zachariah, M., Otto, F., Barnes, C., Philip, S., Kew, S., Vahlberg, M., Singh, R., Heinrich, D., Arrighi, J., Van Aalst, M., Hauser, M., Hirschi, M., Bessenbacher, V., Gudmundsson, L., Beaudoin, H. K., Rodell, M., Li, S., Yang, W., Vecchi, G. A., Harrington, L. J., Lehner, F., Balsamo, G., and Seneviratne, S. I.: Detecting the Human Fingerprint in the Summer 2022 Western–Central European Soil Drought, *Earth System Dynamics*, 15, 131–154, <https://doi.org/10.5194/esd-15-131-2024>, 2024.
- 780 Schwarb, M.: The Alpine Precipitation Climate: Evaluation of a High-Resolution Analysis Scheme Using Comprehensive Rain-Gauge Data, Doctoral Thesis, ETH Zurich, <https://doi.org/10.3929/ethz-a-004121274>, 2000.
- Sen, P. K.: Estimates of the Regression Coefficient Based on Kendall’s Tau, *Journal of the American Statistical Association*, 63, 1379–1389, <https://doi.org/10.1080/01621459.1968.10480934>, 1968.
- Seneviratne, S. I., Lehner, I., Gurtz, J., Teuling, A. J., Lang, H., Moser, U., Grebner, D., Menzel, L., Schroff, K., Vitvar, T., and Zappa,
785 M.: Swiss Prealpine Rietholzbach Research Catchment and Lysimeter: 32 Year Time Series and 2003 Drought Event, *Water Resources Research*, 48, <https://doi.org/10.1029/2011WR011749>, 2012.
- Seneviratne, S. I., Zhang, X., Adnan, M., Badi, W., Dereczynski, C., Di Luca, A., Ghosh, S., Iskander, I., Kossin, J., Lewis, S., Otto, F., Pinto, I., Satoh, M., Vicente-Serrano, S. M., Wehner, M., and Zhou, B.: Weather and Climate Extreme Events in a Changing Climate (Chapter 11), in: *IPCC 2021: Climate Change 2021: The Physical Science Basis. Contribution of Working Group I to the Sixth Assessment Report of the Intergovernmental Panel on Climate Change.*, edited by Masson-Delmotte, V., Zhai, P., Pirani, A., Connors, S. L., Péan, C., Berger, S., Caud, N., Chen, Y., Goldfarb, L., Gomis, M. I., Huang, M., Leitzell, K., Lonnoy, E., Matthews, J. B. R., Maycock, T. K., Waterfield, T., Yelekçi, K., Yu, R., and Zhu, B., pp. 1513–1766, Cambridge University Press, Cambridge, United Kingdom and New York, NY, USA, ISBN 978-1-00-915789-6, 2021.
- 790 Sevruck, B.: Systematischer niederschlagsmessfehler in der Schweiz, in: *Der Niederschlag in der Schweiz*, vol. 31, pp. 65–75, *Beiträge zur Geologie der Schweiz–Hydrologie*, 1985.
- Speich, M. J. R., Bernhard, L., Teuling, A. J., and Zappa, M.: Application of Bivariate Mapping for Hydrological Classification and Analysis of Temporal Change and Scale Effects in Switzerland, *Journal of Hydrology*, 523, 804–821, <https://doi.org/10.1016/j.jhydrol.2015.01.086>, 2015.
- swisstopo: swissALTI3D, <https://www.swisstopo.admin.ch/en/height-model-swissalti3d#Additional-information>, last access: 1 April 2024,
800 2018.
- Teuling, A. J., Van Loon, A. F., Seneviratne, S. I., Lehner, I., Aubinet, M., Heinesch, B., Bernhofer, C., Grünwald, T., Prasse, H., and Spank, U.: Evapotranspiration Amplifies European Summer Drought, *Geophysical Research Letters*, 40, 2071–2075, <https://doi.org/10.1002/grl.50495>, 2013.
- Toreti, A., Bavera, D., Acosta Navarro, J., de Jager, A., Di Ciollo, C., Maetens, W., Magni, D., Masante, D., Mazzeschi, M., Spinoni, J.,
805 Niemeyer, S., Cammalleri, C., and Hrašt Essenfelder, A.: Drought in Europe: August 2022 : GDO Analytical Report, Publications Office of the European Union, ISBN 978-92-76-55855-2, 2022.

- Vaswani, A., Shazeer, N., Parmar, N., Uszkoreit, J., Jones, L., Gomez, A. N., Kaiser, Ł., and Polosukhin, I.: Attention Is All You Need, in: *Advances in Neural Information Processing Systems*, vol. 30, Curran Associates, Inc., 2017.
- 810 Viviroli, D., Mittelbach, H., Gurtz, J., and Weingartner, R.: Continuous Simulation for Flood Estimation in Ungauged Mesoscale Catchments of Switzerland – Part II: Parameter Regionalisation and Flood Estimation Results, *Journal of Hydrology*, 377, 208–225, <https://doi.org/10.1016/j.jhydrol.2009.08.022>, 2009a.
- Viviroli, D., Zappa, M., Gurtz, J., and Weingartner, R.: An Introduction to the Hydrological Modelling System PREVAH and Its Pre- and Post-Processing-Tools, *Environmental Modelling & Software*, 24, 1209–1222, <https://doi.org/10.1016/j.envsoft.2009.04.001>, 2009b.
- 815 Viviroli, D., Zappa, M., Schwanbeck, J., Gurtz, J., and Weingartner, R.: Continuous Simulation for Flood Estimation in Ungauged Mesoscale Catchments of Switzerland – Part I: Modelling Framework and Calibration Results, *Journal of Hydrology*, 377, 191–207, <https://doi.org/10.1016/j.jhydrol.2009.08.023>, 2009c.
- Vorkauf, M., Marty, C., Kahmen, A., and Hiltbrunner, E.: Past and Future Snowmelt Trends in the Swiss Alps: The Role of Temperature and Snowpack, *Climatic Change*, 165, 44, <https://doi.org/10.1007/s10584-021-03027-x>, 2021.
- 820 Weidmann, Y., Gandor, F., and Artuso, R.: Temporale Metadaten swissALTI3D, https://swiss-glaciers.gliacology.ethz.ch/assets/files/documents/weidmann_et_al_2018.pdf, last access: 1 April 2024, 2018.
- Wold, S., Esbensen, K., and Geladi, P.: Principal Component Analysis, *Chemometrics and Intelligent Laboratory Systems*, 2, 37–52, [https://doi.org/10.1016/0169-7439\(87\)80084-9](https://doi.org/10.1016/0169-7439(87)80084-9), 1987.
- Xu, Y., Lin, K., Hu, C., Wang, S., Wu, Q., Zhang, L., and Ran, G.: Deep Transfer Learning Based on Transformer for Flood Forecasting in Data-Sparse Basins, *Journal of Hydrology*, 625, 129 956, <https://doi.org/10.1016/j.jhydrol.2023.129956>, 2023.
- 825 Yan, J., Mu, L., Wang, L., Ranjan, R., and Zomaya, A. Y.: Temporal Convolutional Networks for the Advance Prediction of ENSO, *Scientific Reports*, 10, 8055, <https://doi.org/10.1038/s41598-020-65070-5>, 2020.
- Yao, Y., Rosasco, L., and Caponnetto, A.: On Early Stopping in Gradient Descent Learning, *Constructive Approximation*, 26, 289–315, <https://doi.org/10.1007/s00365-006-0663-2>, 2007.
- 830 Yao, Y., Zhao, Y., Li, X., Feng, D., Shen, C., Liu, C., Kuang, X., and Zheng, C.: Can Transfer Learning Improve Hydrological Predictions in the Alpine Regions?, *Journal of Hydrology*, 625, 130 038, <https://doi.org/10.1016/j.jhydrol.2023.130038>, 2023.
- Zappa, M. and Gurtz, J.: Simulation of Soil Moisture and Evapotranspiration in a Soil Profile during the 1999 MAP-Riviera Campaign, *Hydrology and Earth System Sciences*, 7, 903–919, <https://doi.org/10.5194/hess-7-903-2003>, 2003.
- Zhang, Y., Kang, B., Hooi, B., Yan, S., and Feng, J.: Deep Long-Tailed Learning: A Survey, *IEEE Transactions on Pattern Analysis and Machine Intelligence*, 45, 10 795–10 816, <https://doi.org/10.1109/TPAMI.2023.3268118>, 2023.
- 835 Zhao, W., Gao, Y., Ji, T., Wan, X., Ye, F., and Bai, G.: Deep Temporal Convolutional Networks for Short-Term Traffic Flow Forecasting, *IEEE Access*, 7, 114 496–114 507, <https://doi.org/10.1109/ACCESS.2019.2935504>, 2019.
- Zhou, H., Zhang, S., Peng, J., Zhang, S., Li, J., Xiong, H., and Zhang, W.: Informer: Beyond Efficient Transformer for Long Sequence Time-Series Forecasting, *Proceedings of the AAAI Conference on Artificial Intelligence*, 35, 11 106–11 115, <https://doi.org/10.1609/aaai.v35i12.17325>, 2021.